Geophysical Journal International

Geophys. J. Int. (2016) **205,** 758–775 doi: 10.1093/gji/ggw011
GJI Marine geosciences and applied geophysics

Combination of surface and borehole seismic data for robust target-oriented imaging

Yi Liu,[1] Joost van der Neut,[2] Børge Arntsen[1] and Kees Wapenaar[2]

[1]*Department of Petroleum Engineering and Applied Geophysics, Norwegian University of Science and Technology,* 7491 *Trondheim, Norway. E-mail: yi.liu@ntnu.no*
[2]*Department of Geoscience and Engineering, Delft University of Technology, P.O. Box* 5048, *NL-*2600 *GA Delft, The Netherlands*

Accepted 2016 January 7. Received 2016 January 4; in original form 2015 September 16

SUMMARY

A novel application of seismic interferometry (SI) and Marchenko imaging using both surface and borehole data is presented. A series of redatuming schemes is proposed to combine both data sets for robust deep local imaging in the presence of velocity uncertainties. The redatuming schemes create a virtual acquisition geometry where both sources and receivers lie at the horizontal borehole level, thus only a local velocity model near the borehole is needed for imaging, and erroneous velocities in the shallow area have no effect on imaging around the borehole level. By joining the advantages of SI and Marchenko imaging, a macrovelocity model is no longer required and the proposed schemes use only single-component data. Furthermore, the schemes result in a set of virtual data that have fewer spurious events and internal multiples than previous virtual source redatuming methods. Two numerical examples are shown to illustrate the workflow and to demonstrate the benefits of the method. One is a synthetic model and the other is a realistic model of a field in the North Sea. In both tests, improved local images near the boreholes are obtained using the redatumed data without accurate velocities, because the redatumed data are close to the target.

Key words: Inverse theory; Downhole methods; Interferometry; Wave propagation.

1 INTRODUCTION

Conventional subsurface imaging usually uses active surface seismic data (with sources and receivers at the surface), or various types of VSP data (Vertical Seismic Profile, with either sources or receivers in the subsurface). An image of the subsurface is obtained by applying a depth migration algorithm together with a suitable velocity model. Due to the acquisition geometry, the reflected waves pass through various depths in the earth to the surface. Hence, a velocity model that covers the whole depth section is needed for depth migration. The accuracy of the velocity model has a big impact on the imaging result, especially for deep areas. In practice, one usually only has limited knowledge of the subsurface, and obtaining a good velocity model of the whole area is often a difficult task itself.

On the other hand, seismic interferometry (SI, also called Green's function retrieval) is a data-driven technique that can transform the original data into a sort of virtual data, where physical receivers are turned into virtual sources (Bakulin & Calvert 2006) or vice versa (Curtis *et al.* 2009; Liu *et al.* 2016). This makes it an alternative processing technique for certain types of VSP data (Schuster 2009) to image targeted areas that are difficult to image with the original acquisition geometries. Another advantage of SI is that it is completely data-driven, which is different from other redatuming techniques that rely on prior velocity information of the medium to extrapolate the wavefield downward.

The basic idea of SI is that by crosscorrelating two seismic traces from an active source and sum the result over all sources, we can construct the seismogram that would be recorded at one of the trace's recording positions as if there were a source at the other. It is first described by Claerbout (1968) for horizontally layered media, and is later rediscovered independently by helioseismologists (Duvall *et al.* 1993). Schuster *et al.* (2004) generalize Claerbout's daylight imaging concept to the theory of interferometric seismic imaging and show that it can also be used to migrate multiples in CDP (Common Depth Point) data. The exact form of SI by crosscorrelation (CC) is derived by Wapenaar (2004) for any inhomogeneous lossless medium using reciprocity theorems. Willis *et al.* (2006) show an example of imaging steep salt flanks by creating virtual sources from walk-away VSP data; Bakulin & Calvert (2006) apply SI to image through complex overburdens and develop its field application for sensitive reservoir monitoring. Other approaches to SI have also been proposed. Vasconcelos & Snieder (2008a,b) propose SI by deconvolution and show examples of creating virtual downhole receivers from drill-bit data to image the San Andreas fault. Wapenaar & van der Neut (2010) present SI by multidimensional deconvolution (MDD), which is valid for media with loss and they show that SI by MDD can compensate for one-sided illumination and irregularity of the sources (e.g. variations in their power spectra and unevenly distributed source locations). Minato *et al.* (2011) reconstruct crosswell reflection wavefields without

borehole sources using SI by MDD with singular value decomposition. However, SI by MDD requires wavefield decomposition, which means multicomponent data are necessary, because the up- and downgoing wavefields can be obtained by weighted summation and subtraction of geophone and hydropphone recordings (Amundsen 1993; Amundsen & Reitan 1995). In general, without proper wavefield decomposition, the retrieved responses by SI in practice contain artefacts due to one-sided illumination and limited aperture (Snieder *et al.* 2006) at the summation surface. Comprehensive and systematic comparisons between these different approaches to SI can be found in Snieder *et al.* (2009), Wapenaar *et al.* (2011) and Galetti & Curtis (2012).

As an extension to the classic SI, Curtis *et al.* (2006) and Curtis & Halliday (2010) proposed source–receiver wavefield interferometry (SRI). It retrieves the Green's function from the observations on two closed boundaries, instead of one. Because time-reversal is involved, it holds again only in lossless media. Poliannikov (2011) shows an application using a form of SRI. In his example, the retrieved responses are the downgoing reflections coming from the reflectors above the downhole receivers, so it can be viewed as a way of imaging from below. For practical acquisition geometries with limited apertures and one-sided illumination, the retrieved responses by SRI also contain spurious events. Another approach of imaging from below is shown by van der Neut & Wapenaar (2015), where they use SI by CC of decomposed wavefields, but this still can result in spurious events due to one-sided illumination.

Taking a step beyond SI, another redatuming technique that is generally referred to as the Marchenko method (also called Marchenko focusing) (Broggini *et al.* 2012; Wapenaar *et al.* 2013, 2014; Behura *et al.* 2014) no longer requires the physical presence of a receiver at the position of the virtual source. This implies that one can generate virtual data with any chosen point in the subsurface as a source. However, the method is not completely data-driven, as it requires an estimate of the traveltimes from the virtual source positions to the surface. This means that a macrovelocity model that describes the kinematics of the wavefield is necessary. Various potential applications for Marchenko imaging are suggested by Wapenaar *et al.* (2014). Meles *et al.* (2015) show how to predict and remove internal multiples using the Marchenko scheme and SI. Ravasi *et al.* (2015b, 2016) present a marine data example using a Marchenko scheme.

In this paper, we propose a series of new redatuming schemes that use both surface and borehole seismic data for robust imaging near the borehole. It means that velocity errors, either in the shallow part or near the borehole, will not drastically affect the imaging, as they would for the original data. The virtual data have both sources and receivers at the borehole locations, and then two separate images are calculated—one below the borehole and one above the borehole. By using the direct arrivals from borehole data, this approach joins the benefits of SI and Marchenko imaging. The proposed schemes are completely velocity independent, and need only single-component data for the up–down decomposition. Furthermore, because of the up–down decomposition, the redatumed data contain fewer spurious events than previous data-driven redatuming methods that also use only single-component data.

In the next section, we first explain how to use the surface reflection response to construct the up- and downgoing wavefields at the borehole level. In essence, this is done by finding the focusing functions defined in the Marchenko method, but using the traveltimes measured in the borehole data. Then we construct various redatuming schemes for local imaging from above and from below, respectively. In total, there are four schemes for imaging from above, and two for imaging from below. In the example section, these schemes are tested on two synthetic acoustic data sets, one from a relatively simple synthetic model with a gas cloud in the overburden and the other from a realistic model of a field in the North Sea. The local images are compared with standard images from surface data using both the correct and erroneous velocity models. We then discuss the results, outline directions for further study, and summarize.

2 METHOD

The notation convention used in this paper is similar to what is used in the paper on Marchenko imaging by Wapenaar *et al.* (2014). This makes it easy for the readers to find the detailed derivations of the related equations in the Marchenko method. A spatial position is denoted by $\mathbf{x} = (x_1, x_2, x_3)$, with $x_3 = 0$ on the surface level ∂D_0 and x_3 increasing positively downward. Coordinates at any boundary, for example, at the depth level ∂D_i (which indicates the horizontal borehole depth level in this paper), are denoted as $\mathbf{x}_i = (\mathbf{x}_H, x_{3,i})$, with $\mathbf{x}_H = (x_1, x_2)$. Position $\mathbf{x}_i'$ represents a focusing position at lateral coordinate $\mathbf{x}_H'$ at the depth level ∂D_i, and $\mathbf{x}_0''$ represents a position at lateral coordinate $\mathbf{x}_H''$ at the surface level ∂D_0. Quantities in the frequency domain are indicated with the ˆ above (omitting the variable ω for angular frequency).

We consider only acoustic media, and free-surface multiples are not included (the half-space above the acquisition surface is considered homogeneous). To take the free surface into account, Singh *et al.* (2015) describe Marchenko imaging with the free surface included; for this reason, it is possible to extend the schemes presented here to include free-surface multiples. Throughout this paper, we denote by 'Green's function' the response of an impulsive point source in the actual medium, not in a background medium. When referring to the recorded wavefields in the data, we assume that source deconvolution has been applied, so we can treat the data as measured band-limited Green's functions.

In order not to be confused with Marchenko imaging (which retrieves the reflection response at each depth level of interest and then applies the imaging condition to obtain the image), it is worth to clarify that we aim to retrieve the reflection response only at the borehole depth. Then a conventional depth migration algorithm is applied to obtain a local images above and below the borehole, respectively. To retrieve the reflection response (the redatuming process) for imaging, the focusing functions defined in the Marchenko method is essential for constructing the up–downgoing components in the single-component borehole data. The focusing functions themselves are found by using the direct wavefield and its traveltime from the borehole data, together with the surface reflection response from the surface data. In this way, the proposed redatuming schemes become completely independent of any velocity estimates of the medium.

Now, we start with more details on the up–down decomposition of single-component borehole data using surface reflection data.

2.1 Up–down decomposition of the borehole data

In the Marchenko method, it is shown that the one-way Green's functions is found to be related to the focusing functions via the following relations. For $t \geq t_d(\mathbf{x}_i'|\mathbf{x}_0'')$, where $t_d(\mathbf{x}_i'|\mathbf{x}_0'')$ is the direct arrival time from $\mathbf{x}_0''$ to $\mathbf{x}_i'$,

$$G^-(\mathbf{x}_i'|\mathbf{x}_0'', t) = \int_{\partial D_0}\int_{-\infty}^{t} \mathcal{R}^{\cup}(\mathbf{x}_0''|\mathbf{x}_0, t-t')f_1^+(\mathbf{x}_0|\mathbf{x}_i', t')dt'd\mathbf{x}_0; \quad (1)$$

$$G^{+}(\mathbf{x}_i'|\mathbf{x}_0'',t) = -\int_{\partial D_0}\int_{-\infty}^{t}\mathcal{R}^{\cup}(\mathbf{x}_0''|\mathbf{x}_0,t-t')f_1^{-}(\mathbf{x}_0|\mathbf{x}_i',-t')dt'd\mathbf{x}_0 + f_{1,0}^{+}(\mathbf{x}_0''|\mathbf{x}_i',-t). \quad (2)$$

Here, $G^{-}(\mathbf{x}_i'|\mathbf{x}_0'',t)$ and $G^{+}(\mathbf{x}_i'|\mathbf{x}_0'',t)$ are viewed as the up- and downgoing components of the borehole data received at the horizontal depth level ∂D_i; $\mathcal{R}^{\cup}(\mathbf{x}_0''|\mathbf{x}_0,t)$ is the surface reflection response from the surface data ($^{\cup}$ denotes that this is the reflection response from above, where the downgoing free-surface-related multiples are removed.). The first coordinate vector stands for the receiver position and the second for the position of the source. $f_1^{+}(\mathbf{x}_0|\mathbf{x}_i',t)$ and $f_1^{-}(\mathbf{x}_0|\mathbf{x}_i',t)$ are the down- and upgoing components of the focusing function $f_1(\mathbf{x}_0|\mathbf{x}_i',t)$. For the focusing functions the first coordinate vector stands again for the receiver position, but the second coordinate vector stands for the focal point. The subscript $_0$ indicates the initial estimate, which we will explain shortly. There are two focusing functions, $f_1(\mathbf{x}|\mathbf{x}_i',t)$ and $f_2(\mathbf{x}|\mathbf{x}_0'',t)$, and they are a key element in the Machenko method, but in order to focus on the main idea of this subsection, we will postpone the details of the focusing functions for now. The above equations say that the up- and downgoing components of the borehole data can be calculated, given the focusing functions, the surface reflection response and the traveltime $t_d(\mathbf{x}_i'|\mathbf{x}_0'')$. Since $t_d(\mathbf{x}_i'|\mathbf{x}_0'')$ can be found from the direct arrival's traveltime in the borehole data and we also have the surface reflection response, then the problem becomes to find the focusing functions.

In the Marchenko method, the focusing functions are found by iteratively solving the following equations for $t < t_d(\mathbf{x}_i'|\mathbf{x}_0'')$,

$$f_1^{-}(\mathbf{x}_0''|\mathbf{x}_i',t) = \int_{\partial D_0}\int_{-\infty}^{t}\mathcal{R}^{\cup}(\mathbf{x}_0''|\mathbf{x}_0,t-t')f_1^{+}(\mathbf{x}_0|\mathbf{x}_i',t')dt'd\mathbf{x}_0; \quad (3)$$

$$f_1^{+}(\mathbf{x}_0''|\mathbf{x}_i',-t) = \int_{\partial D_0}\int_{-\infty}^{t}\mathcal{R}^{\cup}(\mathbf{x}_0''|\mathbf{x}_0,t-t')f_1^{-}(\mathbf{x}_0|\mathbf{x}_i',-t')dt'd\mathbf{x}_0. \quad (4)$$

The iterative Marchenko scheme requires an initial estimate to the solution. This estimate is generally obtained by time-reversing the direct wavefield, represented by $G_d(\mathbf{x}_i'|\mathbf{x}_0'',-t)$, which is typically obtained from a smooth macrovelocity model that describes the kinematics of the direct wavefield in Marchenko method. But in our case with given borehole data, this means that we can directly use the direct arrivals to define $G_d(\mathbf{x}_i'|\mathbf{x}_0'',-t)$, and this naturally makes the iterative scheme completely independent of any velocity estimates. This initial estimate of the focusing function can be written as

$$f_{1,0}^{+}(\mathbf{x}_0''|\mathbf{x}_i',t) = f_{2,0}^{-}(\mathbf{x}_i'|\mathbf{x}_0'',t) = G_d(\mathbf{x}_i'|\mathbf{x}_0'',-t). \quad (5)$$

We can now just replace the initial estimate of $f_1^{+}(\mathbf{x}_0''|\mathbf{x}_i',-t)$ on the right-hand side of eq. (2) with $G_d(\mathbf{x}_i'|\mathbf{x}_0'',t)$, so it becomes

$$G^{+}(\mathbf{x}_i'|\mathbf{x}_0'',t) = -\int_{\partial D_0}\int_{-\infty}^{t}\mathcal{R}^{\cup}(\mathbf{x}_0''|\mathbf{x}_0,t-t')f_1^{-}(\mathbf{x}_0|\mathbf{x}_i',-t')dt'd\mathbf{x}_0 + G_d(\mathbf{x}_i'|\mathbf{x}_0'',t). \quad (6)$$

After the focusing functions are found by the iterative Marchenko scheme using the directly measured borehole data, eqs (1) and (6) are used to construct the up- and downgoing components in the borehole data.

Finally, we include more details of the focusing functions. In this paper, they are both defined as a superposition of pressure-normalized downgoing ($^{+}$) and upgoing ($^{-}$) components, such as

$$f_1(\mathbf{x}|\mathbf{x}_i',t) = f_1^{+}(\mathbf{x}|\mathbf{x}_i',t) + f_1^{-}(\mathbf{x}|\mathbf{x}_i',t) \quad (7)$$

and

$$f_2(\mathbf{x}|\mathbf{x}_0'',t) = f_2^{+}(\mathbf{x}|\mathbf{x}_0'',t) + f_2^{-}(\mathbf{x}|\mathbf{x}_0'',t). \quad (8)$$

These focusing functions are solutions to the wave equation in a truncated medium with specific boundary conditions. The truncated medium is identical to the actual medium above ∂D_i, but it is reflection-free below ∂D_i. The focusing conditions read formally as

$$\partial_3 f_1^{+}(\mathbf{x}|\mathbf{x}_i',t)|_{x_3=x_{3,i}} = -\frac{1}{2}\rho(\mathbf{x}_i')\delta(\mathbf{x}_H-\mathbf{x}_H',t)\frac{\partial\delta(t)}{\partial t} \quad (9)$$

and

$$\partial_3 f_2^{-}(\mathbf{x}|\mathbf{x}_0'',t)|_{x_3=x_{3,0}} = \frac{1}{2}\rho(\mathbf{x}_0'')\delta(\mathbf{x}_H-\mathbf{x}_H'',t)\frac{\partial\delta(t)}{\partial t}. \quad (10)$$

The difference between the two focusing functions is that $f_1(\mathbf{x}|\mathbf{x}_i',t)$ focuses at $\mathbf{x}_i'$ in the subsurface and $f_2(\mathbf{x}|\mathbf{x}_0'',t)$ focuses at $\mathbf{x}_0''$ at the surface. The two focusing functions are mutually related via

$$f_1^{+}(\mathbf{x}_0''|\mathbf{x}_i',t) = f_2^{-}(\mathbf{x}_i'|\mathbf{x}_0'',t); \quad (11)$$

and

$$-f_1^{-}(\mathbf{x}_0''|\mathbf{x}_i',-t) = f_2^{+}(\mathbf{x}_i'|\mathbf{x}_0'',t). \quad (12)$$

2.2 Imaging from above

Assuming a horizontal borehole, we define the idea of imaging from above as to retrieve the reflection response from above (of the medium below the borehole), as if the medium above the borehole is reflection-free. Then a conventional depth migration algorithm is applied to the retrieved reflection response using only a local velocity model to produce an image below the borehole. In other words, we aim to use the original borehole data set (sources at the surface and receivers in the borehole) and the surface data set (source and receiver at the surface) to create a virtual data set with both sources and receivers in the borehole, above which the medium is reflection-free.

It has been shown that such virtual reflection response $\mathcal{R}^{\cup}(\mathbf{x}_i'|\mathbf{x}_i,t)$ is related to the up–downgoing wavefields via (Amundsen 2001; Wapenaar *et al.* 2011)

$$G^{-}(\mathbf{x}_i'|\mathbf{x}_0'',t) = \int_{\partial D_i}\int_{-\infty}^{+\infty}\mathcal{R}^{\cup}(\mathbf{x}_i'|\mathbf{x}_i,t')G^{+}(\mathbf{x}_i|\mathbf{x}_0'',t-t')dt'd\mathbf{x}_i, \quad (13)$$

so $\mathcal{R}^{\cup}(\mathbf{x}_i'|\mathbf{x}_i,t)$ can be solved if the up–down wavefields are known. This typically requires multicomponent data for the up-down decomposition (Amundsen & Reitan 1995). For single-component data, an alternative is to approximate the downgoing $G^{+}(\mathbf{x}_i|\mathbf{x}_0'',t)$ with the direct arrivals in the borehole data and use the remaining data for the upgoing $G^{-}(\mathbf{x}_i|\mathbf{x}_0'',t)$ (van der Neut *et al.* 2016), such as

$$G^{+}(\mathbf{x}_i|\mathbf{x}_0'',t) \approx G_d(\mathbf{x}_i|\mathbf{x}_0'',t), \quad (14)$$

and

$$G^{-}(\mathbf{x}_i'|\mathbf{x}_0'',t) \approx G(\mathbf{x}_i'|\mathbf{x}_0'',t) - G_d(\mathbf{x}_i'|\mathbf{x}_0'',t), \quad (15)$$

so eq. (13) becomes

$$G(\mathbf{x}_i'|\mathbf{x}_0'', t) - G_d(\mathbf{x}_i'|\mathbf{x}_0'', t) \approx \int_{\partial D_i}\int_{-\infty}^{+\infty} \mathcal{R}^{\cup}(\mathbf{x}_i'|\mathbf{x}_i, t')G_d(\mathbf{x}_i|\mathbf{x}_0'', t-t')dt'd\mathbf{x}_i. \quad (16)$$

This scheme only uses borehole data. The retrieved response $\mathcal{R}^{\cup}(\mathbf{x}_i'|\mathbf{x}_i, t)$ contains spurious events related to the approximations made in eqs (14) and (15). But when the multiple reflections in the subsurface are not strong, the up–down wavefield approximation in eqs (14) and (15) is sufficient for retrieving the reflection response from above to image close to the borehole. We will later see an example of this in the numerical section.

Next, we show the schemes that use both surface and borehole data. As shown in the previous subsection, namely that the up- and downgoing components in the borehole data can be computed once the focusing functions are found, we can rewrite the exact scheme in eq. (13) as

$$\Psi\left[\int_{\partial D_0}\widehat{\mathcal{R}^{\cup}}(\mathbf{x}_0''|\mathbf{x}_0)\widehat{f_1^+}(\mathbf{x}_0|\mathbf{x}_i')d\mathbf{x}_0\right] = \int_{\partial D_i}\widehat{\mathcal{R}^{\cup}}(\mathbf{x}_i'|\mathbf{x}_i)\left\{\Psi\left[-\int_{\partial D_0}\widehat{\mathcal{R}^{\cup}}(\mathbf{x}_0''|\mathbf{x}_0''')\widehat{f_1^-}^*(\mathbf{x}_0'''|\mathbf{x}_i)d\mathbf{x}_0'''\right] + \widehat{G}_d(\mathbf{x}_i|\mathbf{x}_0'')\right\}d\mathbf{x}_i, \quad (17)$$

by using eqs (1) and (6). Here, to make the equation relatively short and easier to interpret, we decide to switch to the frequency domain (indicated by the $\hat{}$ above the quantities) and introduce an operator Ψ. The operator Ψ first inverse Fourier transforms the data, then applies a time window which passes data only for $t \geq t_d(\mathbf{x}_i'|\mathbf{x}_0'')$, and then Fourier transforms the result back to the frequency domain. In this equation, $\widehat{\mathcal{R}^{\cup}}(\mathbf{x}_i'|\mathbf{x}_i)$ is the unknown, $\widehat{f_1^+}(\mathbf{x}_0|\mathbf{x}_i')$ is found by iteratively solving eqs (3) and (4) using the direct wavefield in the borehole data as the initial solution as explained in the previous subsection. $\widehat{\mathcal{R}^{\cup}}(\mathbf{x}_0''|\mathbf{x}_0)$ is the surface reflection data and $\widehat{G}_d(\mathbf{x}_i|\mathbf{x}_0'')$ is the direct arrivals from the borehole data. The equation is then solved per frequency, using a least-squares approach, for example. The retrieved $\mathcal{R}^{\cup}(\mathbf{x}_i'|\mathbf{x}_i, t)$ under this scheme does not contain any spurious events related to the internal multiples from the overburden.

In practice, solving for the focusing functions is not always trivial. Various factors such as the accuracy of surface reflection response, wavelet deconvolution, source/receiver deghosting and attenuation all need to be taken into account (van der Neut *et al.* 2015). In the light of these practical aspects, we suggest an approximate alternative. This is done by using eqs (1), (5), and the direct wave approximation for $G^+(\mathbf{x}_i|\mathbf{x}_0'', t)$ in eq. (14) for substitution in eq. (13), which gives

$$\Psi\left[\int_{\partial D_0}\widehat{G}_d^*(\mathbf{x}_i'|\mathbf{x}_0)\widehat{\mathcal{R}^{\cup}}(\mathbf{x}_0''|\mathbf{x}_0)d\mathbf{x}_0\right] \approx \int_{\partial D_i}\widehat{\mathcal{R}^{\cup}}(\mathbf{x}_i'|\mathbf{x}_i)\widehat{G}_d(\mathbf{x}_i|\mathbf{x}_0'')d\mathbf{x}_i. \quad (18)$$

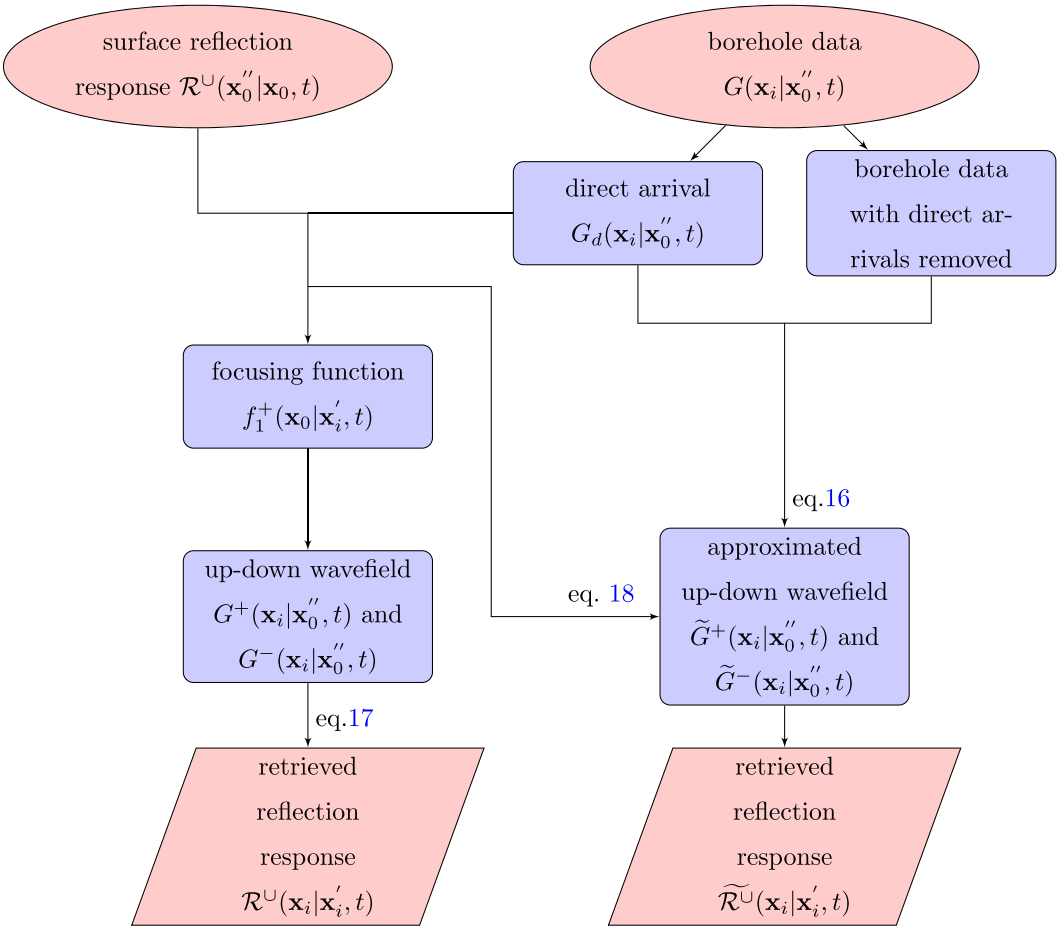

Figure 1. Flow chart for imaging from above. The ellipses indicate the input and the trapezia indicate the output. The intermediate steps are indicated by the boxes. The ˜ above the symbols indicates approximation.

This scheme can be viewed as the result from the first iteration of the iterative Marchenko scheme in finding the focusing function. With this scheme, the retrieved response will contain some spurious events related to internal multiples. But this is still a good complement to the scheme based on the borehole data only (eq. 16), because in addition to being completely data-driven, it also incorporates information from the surface, and the approximation for the upgoing wavefield (eq. 15) is avoided.

Finally, one more alternative scheme is to combine eqs (16) and (18) (or analogously, eqs 13 and 17), and solve for $\mathcal{R}^{\cup}(\mathbf{x}_i', \mathbf{x}_i, t)$, using MDD, for example. This joint system of equations reads, in matrix form:

$$\begin{bmatrix} \mathbf{U}_1 \\ \alpha \mathbf{U}_2 \end{bmatrix} = \mathbf{R} \begin{bmatrix} \mathbf{D}_1 \\ \alpha \mathbf{D}_1 \end{bmatrix}, \tag{19}$$

where $\mathbf{U}_1$ and $\mathbf{U}_2$ correspond to the left-hand sides of eqs (16) and (18), and $\mathbf{D}_1$ to the counterparts on the right-hand sides. Here, α is a user-defined scalar weight, which could be frequency-dependent, depending on the characteristics of both subproblems and how much weight one wants for the surface data. Inverting this joint scheme might be better than inverting a single scheme (as eq. 16 or 18). Because in practice, there can be various hardware related issues in both data sets, such as sensor coupling, malfunctioning sensors, etc. In addition, the high-frequency components in the borehole data can have a better signal-to-noise ratio than the same frequency components in the surface data (due to less attenuation), and borehole data may have higher propagation angles for imaging the structures that could not be found in the surface data. Therefore, this joint inversion approach could help to merge the data sets.

Fig. 1 illustrates the processing flow for the schemes described in this subsection. To summarize, both eq. (17) remove all downgoing multiples coming from the overburden using single-component borehole and surface data with an iterative Marchenko approach; eqs (16), (18) and (19) do not completely remove all such downgoing multiples, but they are straightforward to implement and still sufficient for imaging near the borehole (which we will demonstrate with the numerical examples). Another benefit of these schemes is that the retrieved reflection responses are redatumed in a data-driven way to the borehole level for imaging downwards, such that one does not need any velocity information of the overburden. This is also an acknowledged aspect in the virtual source method by Bakulin & Calvert (2006), but our approach requires less information from the data (only single-component recordings).

2.3 Imaging from below

Again, assuming a horizontal borehole, we define imaging from below as to retrieve the reflection response from below (of the medium above the borehole), as if the medium below the borehole is reflection-free. Then an image above the borehole is obtained by applying a conventional depth migration algorithm to the retrieved

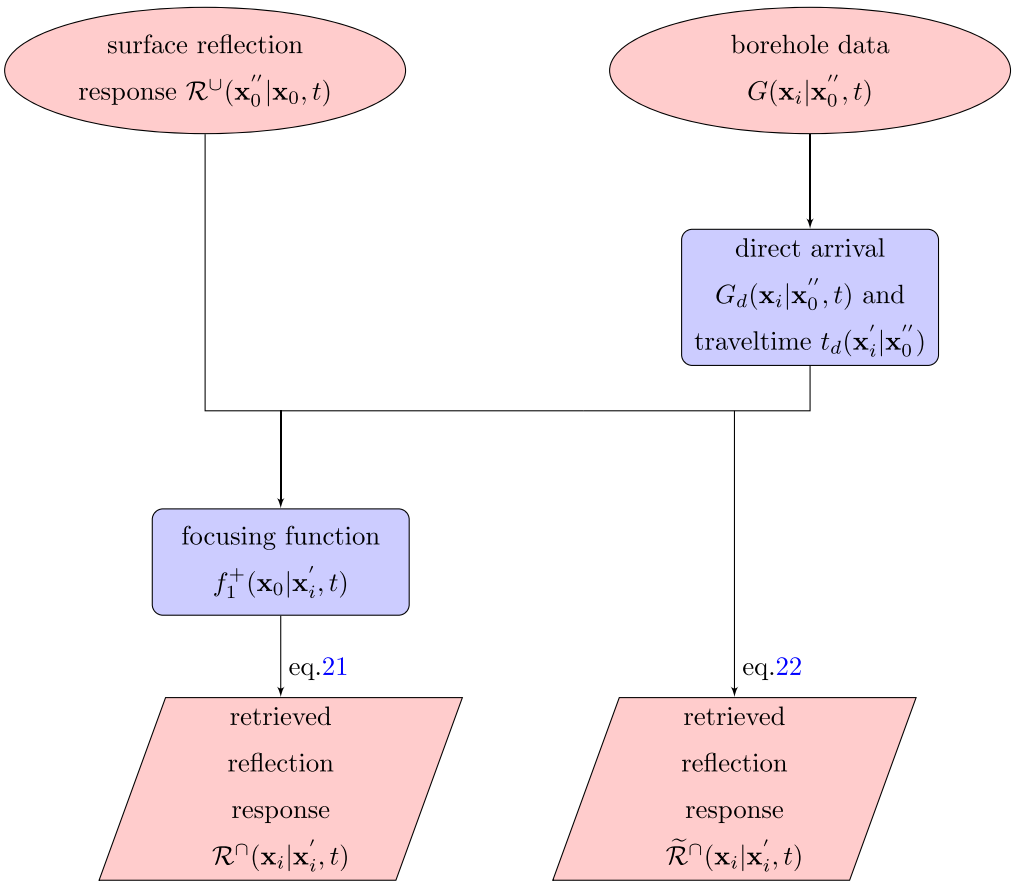

Figure 2. Flow chart for imaging from below. The ellipses indicate the input and the trapezia indicate the output. The intermediate steps are indicated by the boxes. The˜ above the symbols indicates approximation.

response, using a local velocity model above the borehole. In other words, we aim to use borehole data and surface data to create a virtual data set with both sources and receivers in the borehole, below which the medium is reflection-free.

This reflection response from below $\mathcal{R}^{\cap}(\mathbf{x}_i'|\mathbf{x}_i,t)$ ($^{\cap}$ denotes that this is the reflection response from below) is shown (Wapenaar *et al.* 2014) to be related to the focusing functions via

$$f_2^{+}(\mathbf{x}_i'|\mathbf{x}_0'',t)=\int_{\partial D_i}\int_{-\infty}^{+\infty}\mathcal{R}^{\cap}(\mathbf{x}_i'|\mathbf{x}_i,t')f_2^{-}(\mathbf{x}_i|\mathbf{x}_0'',t-t')dt'd\mathbf{x}_i; \tag{20}$$

for this reason, to solve for $\mathcal{R}^{\cap}(\mathbf{x}_i'|\mathbf{x}_i,t)$, we need the focusing functions $f_2^{\pm}$. But first, we can rewrite the above equation in terms of f_1^{+}, using the mutual relation of the focusing functions from eq. (12), and the relation from eq. (3), such as

$$-\left\{\Theta\left[\int_{\partial D_0}\widehat{f_1^{+}}(\mathbf{x}_0|\mathbf{x}_i')\widehat{\mathcal{R}^{\cup}}(\mathbf{x}_0''|\mathbf{x}_0)d\mathbf{x}_0\right]\right\}^{*}=\int_{\partial D_i}\widehat{\mathcal{R}^{\cap}}(\mathbf{x}_i'|\mathbf{x}_i)\widehat{f_1^{+}}(\mathbf{x}_0''|\mathbf{x}_i)d\mathbf{x}_i, \tag{21}$$

where the superscript * denotes conjugation. This equation gives the exact scheme for retrieving $\mathcal{R}^{\cap}(\mathbf{x}_i'|\mathbf{x}_i,t)$. Again, here we switch to the frequency domain (indicated by the $\widehat{\ }$) for previously stated reasons. Similar to Ψ, the operator Θ first inverse Fourier transforms the result, then applies a time window which passes data only for $t<t_d(\mathbf{x}_i'|\mathbf{x}_0'')$, and then Fourier transforms the result back to the frequency domain. In this equation, $\widehat{f_1^{+}}(\mathbf{x}_0''|\mathbf{x}_i)$, is found by the same procedure as explained in the previous two subsections, and $\mathcal{R}^{\cup}(\mathbf{x}_0''|\mathbf{x}_0)$ is the surface reflection response. Then, the unknown $\widehat{\mathcal{R}^{\cap}}(\mathbf{x}_i'|\mathbf{x}_i)$ can be solved per frequency, using a least-squares approach, for example. As the first iteration of the Marchenko scheme for $f_1^{+}(\mathbf{x}_0|\mathbf{x}_i',t)$, an approximate alternative scheme is

$$-\left\{\Theta\left[\int_{\partial D_0}\widehat{G}_d^{*}(\mathbf{x}_i'|\mathbf{x}_0)\widehat{\mathcal{R}^{\cup}}(\mathbf{x}_0''|\mathbf{x}_0)d\mathbf{x}_0\right]\right\}^{*}\approx\int_{\partial D_i}\widehat{\mathcal{R}^{\cap}}(\mathbf{x}_i'|\mathbf{x}_i)\widehat{G}_d^{*}(\mathbf{x}_i|\mathbf{x}_0'')d\mathbf{x}_i, \tag{22}$$

where eq. (5) is used. We note that this scheme resembles the imaging from below method by Poliannikov (2011), because an approximate solution of $\mathcal{R}^{\cap}(\mathbf{x}_i'|\mathbf{x}_i,t)$ by CC is equivalent to his result (which he derived from SRI). This CC solution is obtained by writing out the normal equation of eq. (22) and approximate the solution with the left-hand side of the normal equation. But we see now that because of the substitution of eq. (5), either solving eq. (22) by MDD or by CC results in spurious events in the retrieved $\mathcal{R}^{\cap}(\mathbf{x}_i'|\mathbf{x}_i,t)$. Those spurious events related to the upgoing internal multiples can be removed by using the exact form in eq. (21). Nevertheless, when

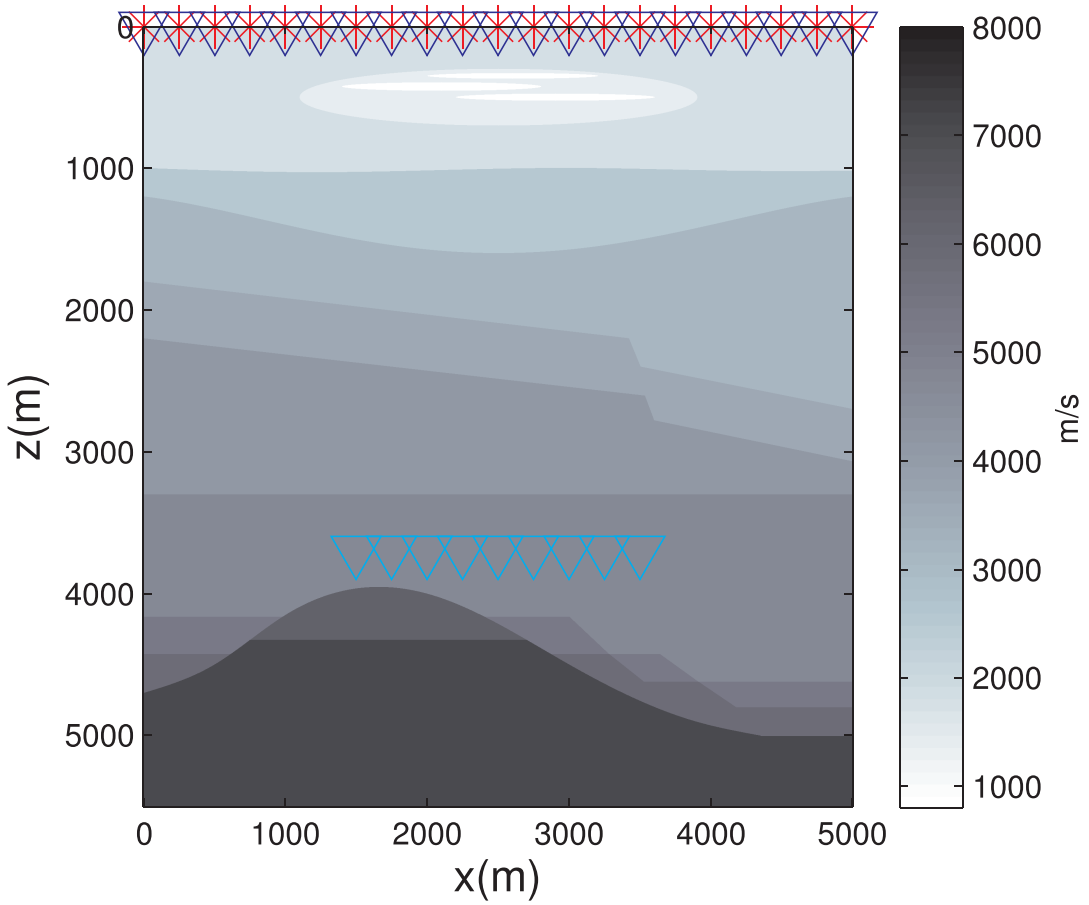

Figure 3. *P*-wave velocity model and data sets geometries. The stars denote sources and the triangles denote receivers. Every 10th source and receiver is plotted. Letters *x* and *z* represent horizontal and vertical directions, respectively.

the internal multiples are not strong, eq. (22) is a simple and sufficient scheme for imaging close to the borehole. The flow chart in Fig. 2 illustrates the two schemes.

3 NUMERICAL EXAMPLES

In the numerical experiments, we use two 2-D acoustic models to test the redatumig schemes and to observe to what extent velocities errors affect the local images, as compared to conventional surface images (images obtained from surface data alone). The first model is a synthetic model with a gas cloud in the shallow part, and the second model is a realistic model of a field in the North Sea. A finite-difference method (Thorbecke & Draganov 2011) is used for generating the data sets. After redatuming, a pre-stack depth migration algorithm (Thorbecke *et al.* 2004) is used for imaging. For each model, we generate two data sets—a surface data set (with sources and receivers at the surface) and a borehole data set (with sources at the surface and receivers in the borehole). The surface data are modeled as the response to an input band-limited spike with a maximum frequency of 55 Hz, and the borehole data are modeled with a Ricker wavelet with a peak frequency of 20 Hz. The free surface is replaced by an absorbing boundary.

3.1 Example 1: local imaging below a gas cloud

Fig. 3 shows the *P*-wave velocity model and the input data sets geometries. The model is 5 by 5.5 km, with a grid sampling of 2.5 m. It consists of a low-velocity gas cloud in the shallow part (around 0.5 km depth) and a syncline alongside some faults in the deeper part (below 4 km). The borehole data set has 201 sources at the surface and 81 receivers at 3.7 km depth. The surface data set has 201 sources and receivers. The source and receiver intervals are 25 m. Examples of the common-source gathers from both data sets are shown in Fig. 4. The time window is found by the traveltime $t_d(\mathbf{x}_i'|\mathbf{x}_0'')$ in the borehole data and it is indicated by the dashed line in the figure.

3.1.1 Redatumed reflection responses

To retrieve the reflection response from above, $\mathcal{R}^{\cup}(\mathbf{x}_i'|\mathbf{x}_i, t)$, we test four schemes, namely, eqs (16), (18), (17) and (19). Fig. 5 shows the comparison between the redatumed reflection responses (in red) and the reference response (in blue). The reference response (direct arrivals muted) is modeled with a homogeneous overburden above the borehole. The reference source position is at $x = 2500$ m at the depth of 3.7 km. An overall scalar is applied on the retrieved responses to scale with the reference response. In addition, a local extra gain is applied both on the reference and retrieved responses for $t > 1s$ to amplify the internal multiples.

For the first scheme (eq. 16), only the borehole data set is used, and the scheme is closely related to the virtual source method by Bakulin & Calvert (2006), where their result is obtained by the CC of the left-hand side of eq. (16) with the direct arrivals on the right-hand side. Here, we solve eq. (16) per frequency by MDD.

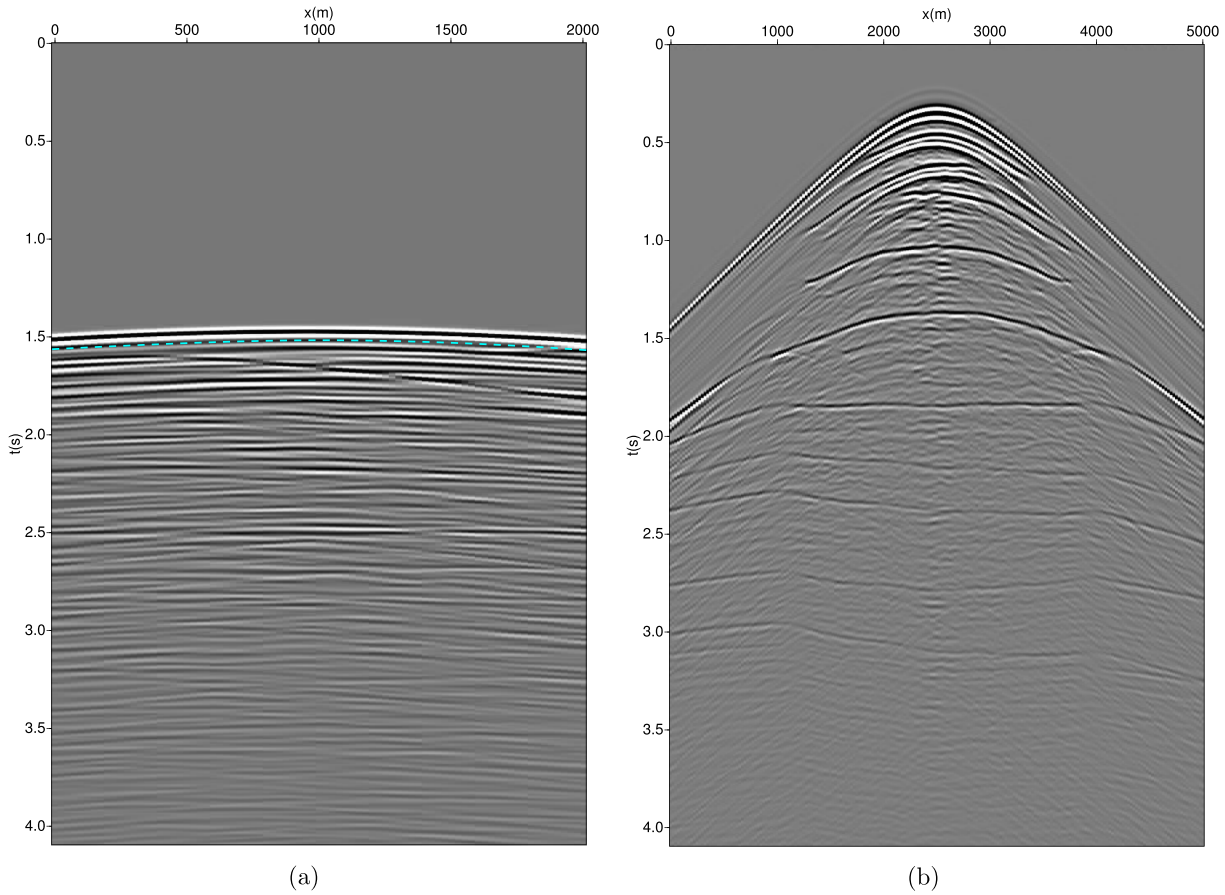

Figure 4. An example of the common-source gathers from (a) borehole data and (b) surface data (the direct arrivals are muted). The dashed line indicates the time window found by the direct arrival's traveltime in the borehole data.

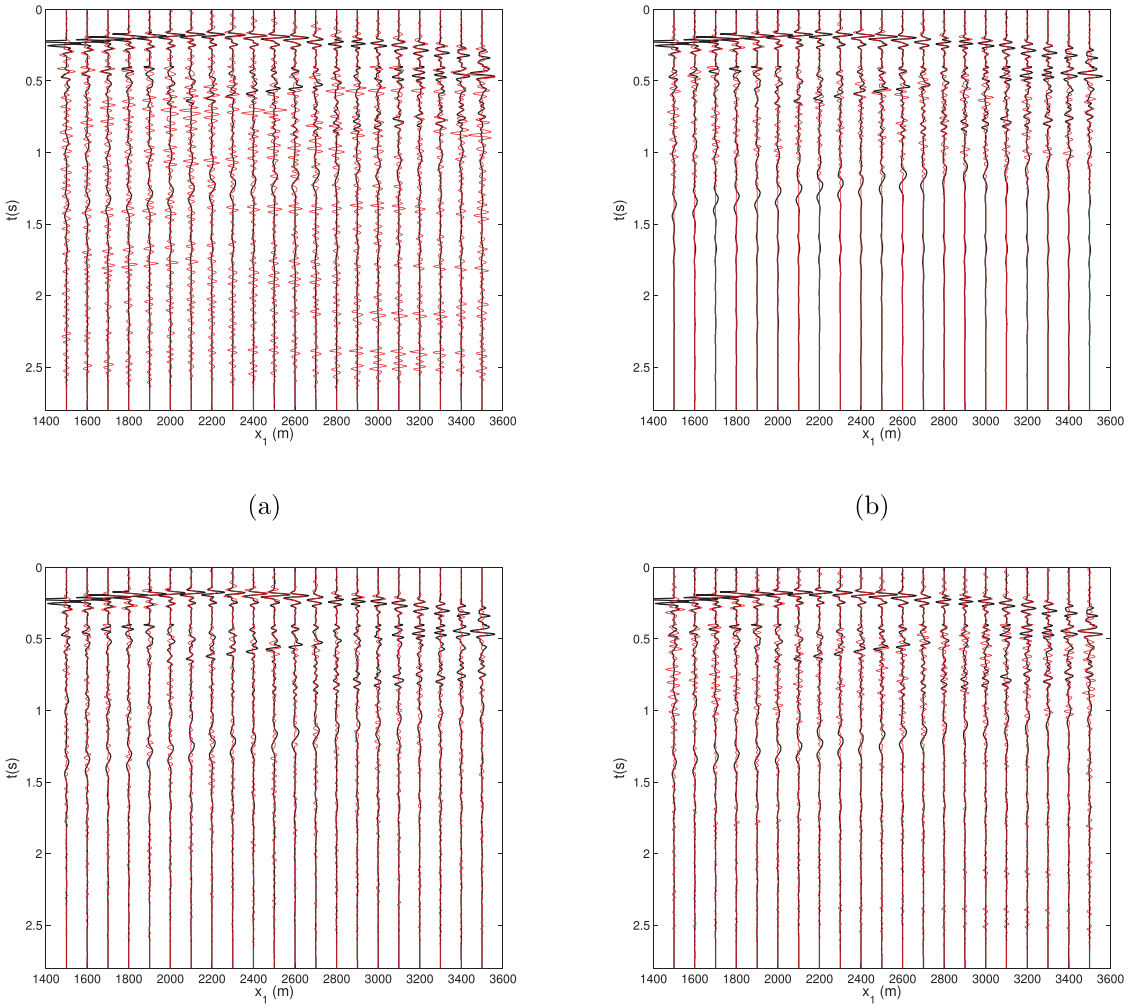

Figure 5. Redatumed reflection responses for imaging from above. Trace comparison between the retrieved responses and the reference responses, using (a) single-component borehole data only (eq. 16), (b) surface reflection data and the direct arrivals in the borehole data (eq. 18), (c) the same input as (b) but the focusing functions are found by an iterative Marchenko method (eq. 17) and (d) a joint scheme of (a) and (b) (eq. 19). The colour black indicates the modeled reference response and the colour red indicates the redatumed response. An overall scale is applied on the retrieved responses and a local scalar gain is applied for $t > 1$ s to amplify the multiples. The low-frequency events in the reference response are due to the imperfect absorbing boundary in the forward modelling. Every fourth trace is plotted.

For the second scheme (eq. 18), the surface data set is included to redatum the direct arrivals in the borehole data for approximating the upgoing component in the exact scheme. For the third scheme (eq. 17), the input is the same as for the second scheme, but an iterative Marchenko method (Wapenaar *et al.* 2014) is used to find the focusing functions, with the direct traveltime $t_d(\mathbf{x}_i'|\mathbf{x}_0'')$ from the borehole data set. For the fourth scheme (eq. 19), we joined the schemes one and two with an α of 2. All equations are solved using a damped least-squares approach (Menke 1989).

By comparing the traces in Fig. 5, it can be observed that panel (a) has the most spurious events, but mainly in the later arrivals. This is because the approximations in eqs (14) and (15) do not account for the internal multiples. These downgoing events are almost completely removed in panel (c), where the up–down wavefields are properly decomposed in the exact scheme.

To retrieve the reflection response from below, $\mathcal{R}^{\cap}(\mathbf{x}_i'|\mathbf{x}_i, t)$, we test two schemes, namely (eqs 22 and 21). Fig. 6 shows the comparison between the redatumed result in red and the reference response in black. The reference response (direct arrivals muted) is modeled with a homogeneous underburden below the borehole. The reference source position is $x = 2500$ m at the depth of 3.7 km.

In the trace comparison, an overall scalar factor is applied on the redatumed result, and an extra gain is applied for $t > 3$ s to amplify the multiples. One can see that the second scheme which uses the focusing functions results in a better match, both in terms of the amplitude and fewer spurious events. Nevertheless, the first scheme still recovers the nearby reflectors well.

3.1.2 *Target images*

Next, the redatumed reflection responses are used for imaging from above and from below the borehole, respectively. First, the true local velocities are used for migration. The results are shown in Figs 7 and 8. We see that the nearby reflectors are all clearly imaged in

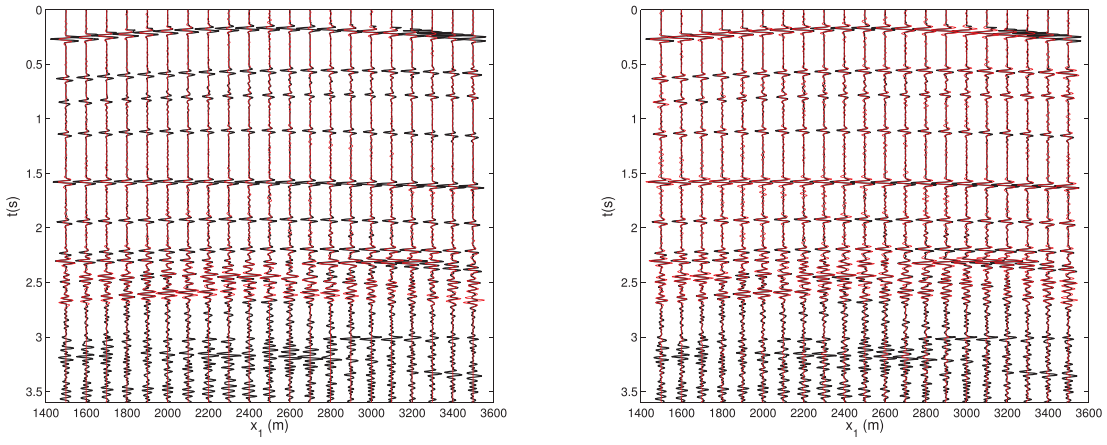

Figure 6. Redatumed reflection responses for imaging from below. Trace comparison between the retrieved responses and the reference responses, using (a) direct arrivals in the borehole data, together with the surface reflection response (eq. 22) and (b) surface reflection response and the focusing functions (eq. 21, using the direct arrivals in the borehole data and the surface reflection response as input to the iterative Marchenko method). An overall scale is applied on the retrieved responses and a local gain is applied for $t > 3$ s to amplify the multiples. Every fourth trace is plotted.

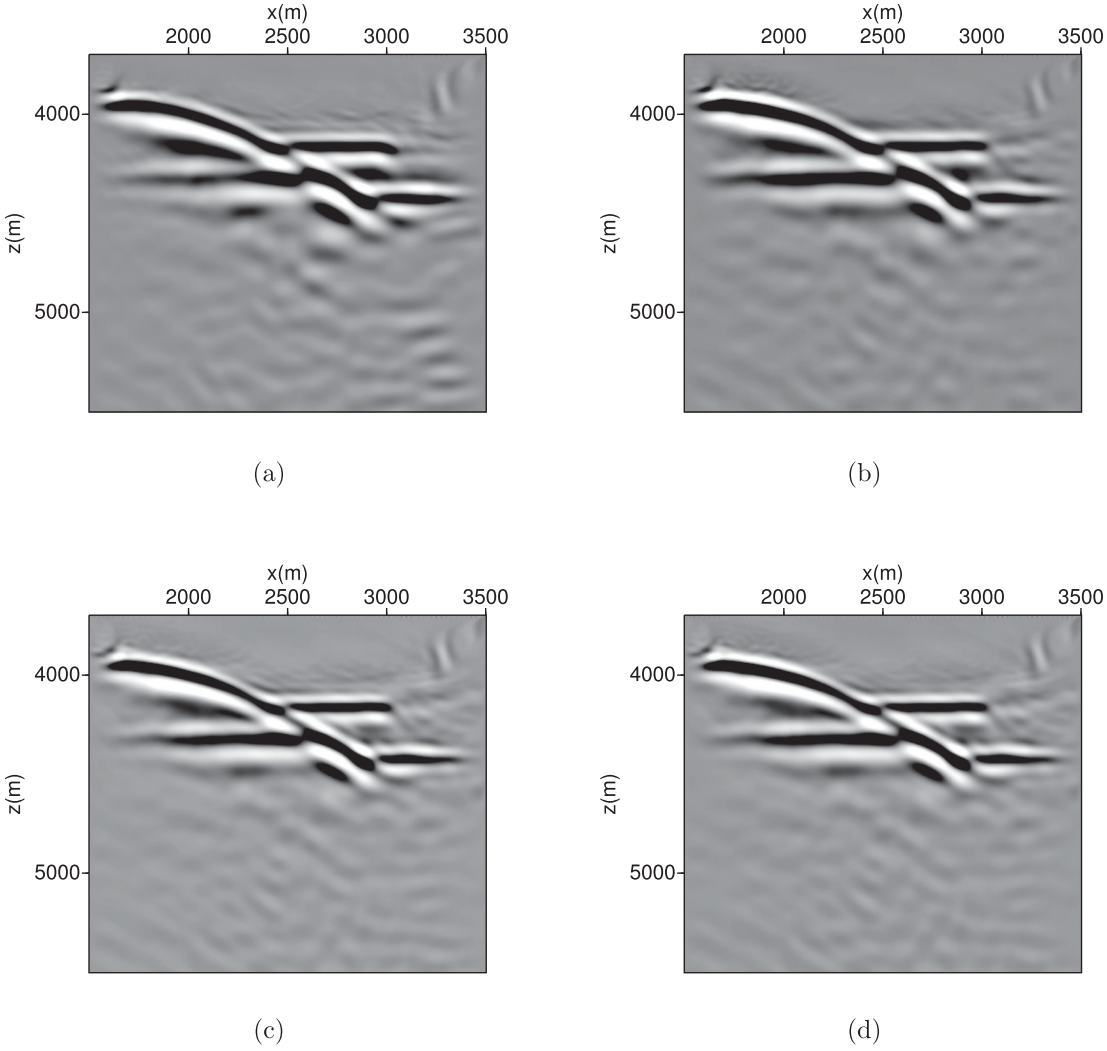

Figure 7. Migrated images from above with the correct local velocities. The data for migration are redatumed from (a) the borehole data only scheme (eq. 16), (b) the borehole and surface data scheme without the full focusing functions (18), (c) as (b) but with the full focusing functions (eq. 17) and (d) the joint scheme of (a) and (b) (eq. 19).

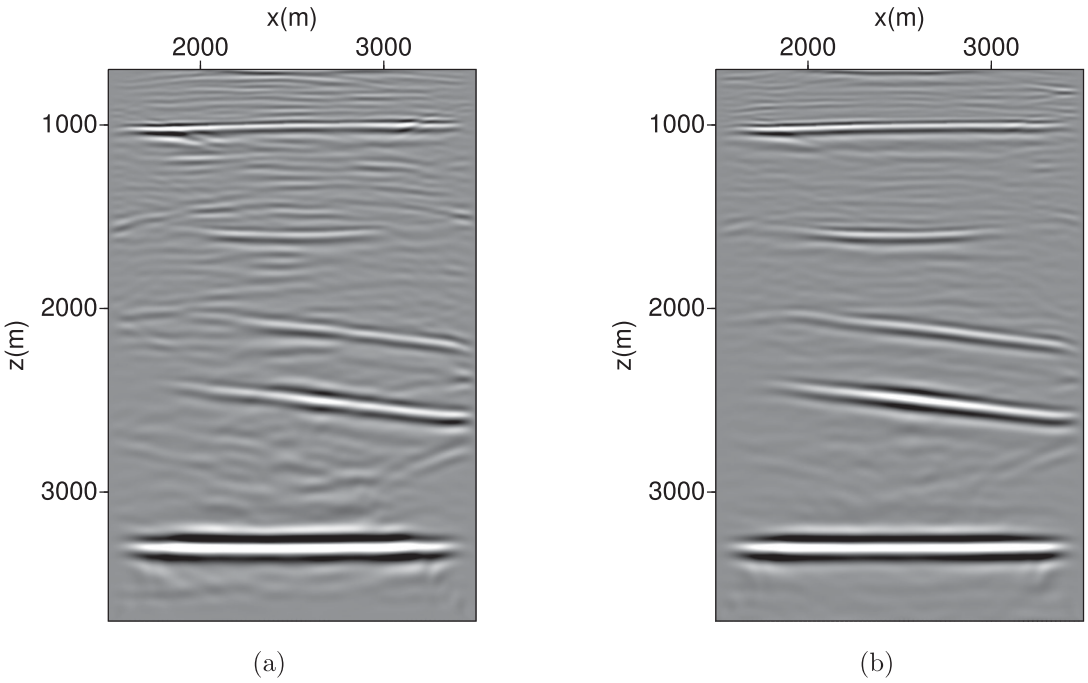

(a) (b)

Figure 8. Migrated images from below with the correct local velocities. The data for migration are redatumed from (a) the borehole and surface data scheme without the full focusing functions (eq. 22), (b) as (a) but with the correct focusing functions (eq. 21).

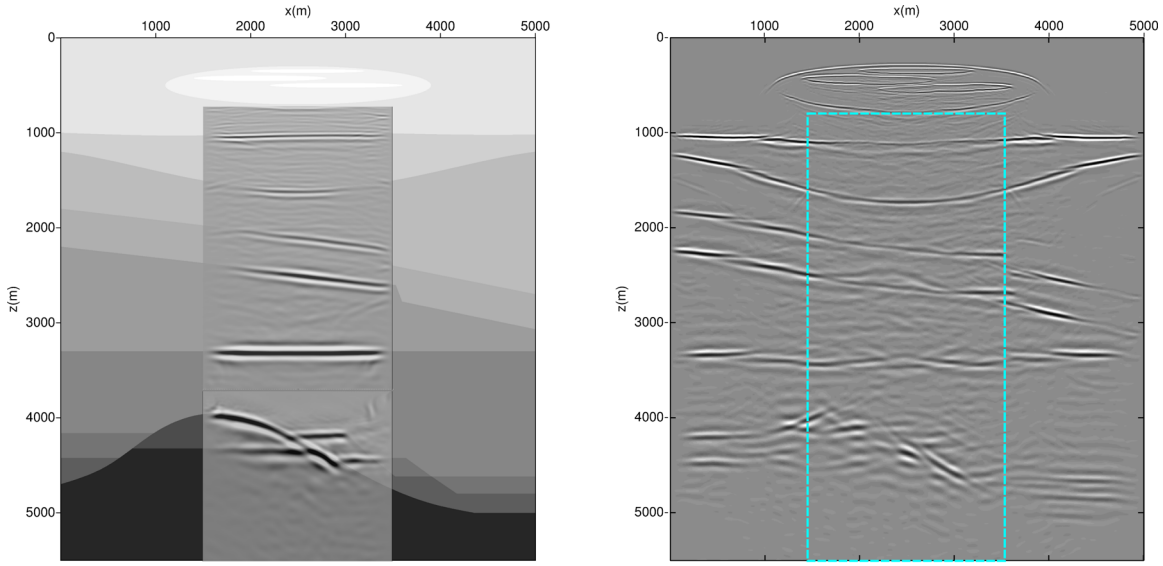

(a) (b)

Figure 9. Image comparison of (a) target images from the redatumed data using the focusing functions (eqs 17 and 21) and (b) surface image from original surface reflection data. The dashed box highlights the target area. The true velocity model is used for migration.

both figures, even though they are hindered by the gas cloud at the surface. Furthermore, no medium parameter of the gas cloud is needed for imaging the structures underneath. In terms of the influence of internal multiples on imaging, we see that it is the most obvious in the image from below in Fig. 8(b) where the correct focusing function is computed. In this case, the strong internal multiples from the underburden are removed.

To test the robustness of the target images to velocity errors and to compare with conventional surface images, we first use a smoothed true velocity model to migrate the redatumed results by the schemes in eqs (17) and (21) (corresponding to Figs 5c and 6b). The original surface data are also migrated using the same smoothed model. The result is shown in Fig. 9. We can see already that surface image struggles to image the deep reflectors because of the gas cloud, while the target images position these reflectors clearly and correctly. To further demonstrate the benefit of this data-driven redatuming, a 1-D linear velocity model is used and the result is shown in Fig. 10. Now the deep reflectors can barely be recognized in the surface image, while, even though less focused, they remain clearly present in the target images. In addition, the reflectors near the borehole are less mispositioned than in the surface image.

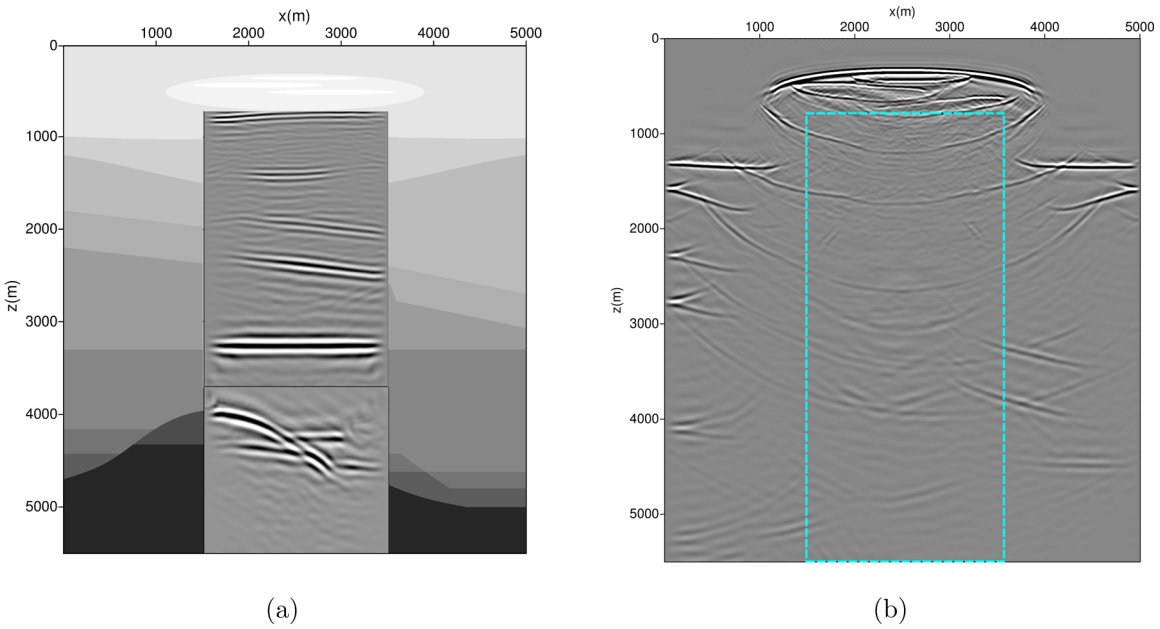

Figure 10. Image comparison of (a) target images from the redatumed results and (b) surface image from original surface reflection data. The dashed box highlights the target area. A simple 1-D linear velocity model is used for migration.

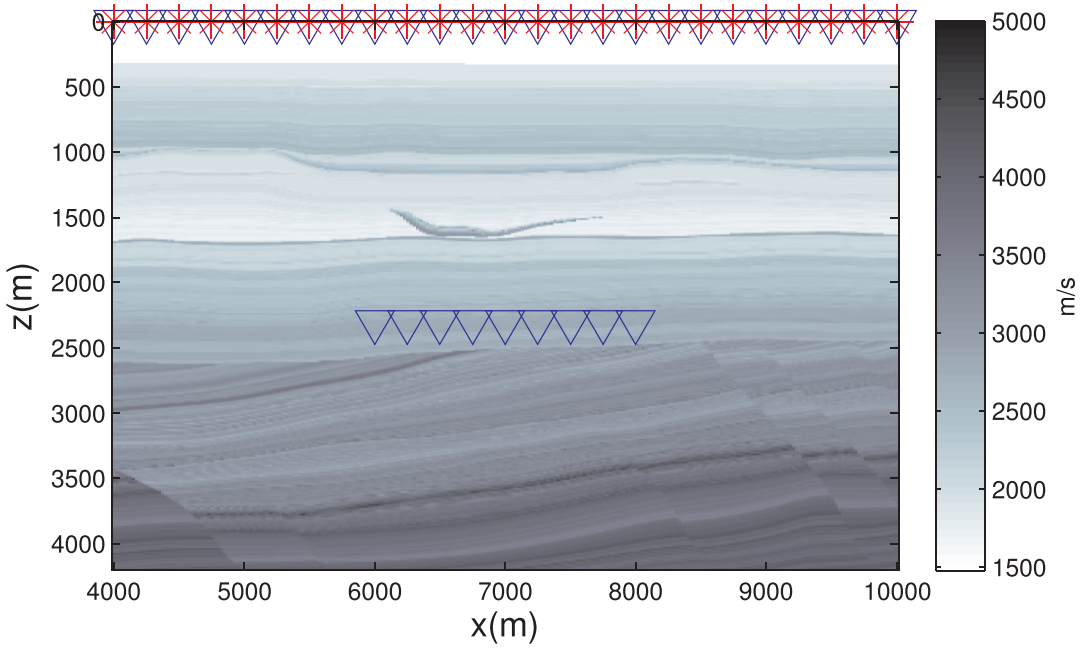

Figure 11. *P*-wave velocity model and data sets geometries. The stars denote sources and the triangles denote receivers.

3.2 Example 2: a realistic model from the North Sea

Fig. 11 shows the 2-D *P*-wave velocity model and the input data sets geometries. The model dimension is 6 by 4.2 km, with a grid sampling of 5 m. There is a seagull-shaped low-velocity anomaly at around 1.5 km depth. The borehole data set has 241 sources at the surface and 81 receivers at 2.3 km depth. The surface data set has 241 sources and receivers. The source and receiver intervals are 25 m. Examples of the common-source gathers from both data sets are shown in Fig. 12.

3.2.1 Redatumed reflection response

Figs 13 and 14 show the redatumed reflection responses for imaging from above and from below, respectively. An overall scalar factor is applied on the result. In addition, an extra gain is applied both on the reference and retrieved responses for $t > 1.2$ s in the figures to amplify the internal multiples. We observe that all schemes result in good kinematic matches for the reflectors near the borehole. In Fig. 13(a) where only the borehole data are used in the redatuming scheme, the later arrivals do not match the reference response

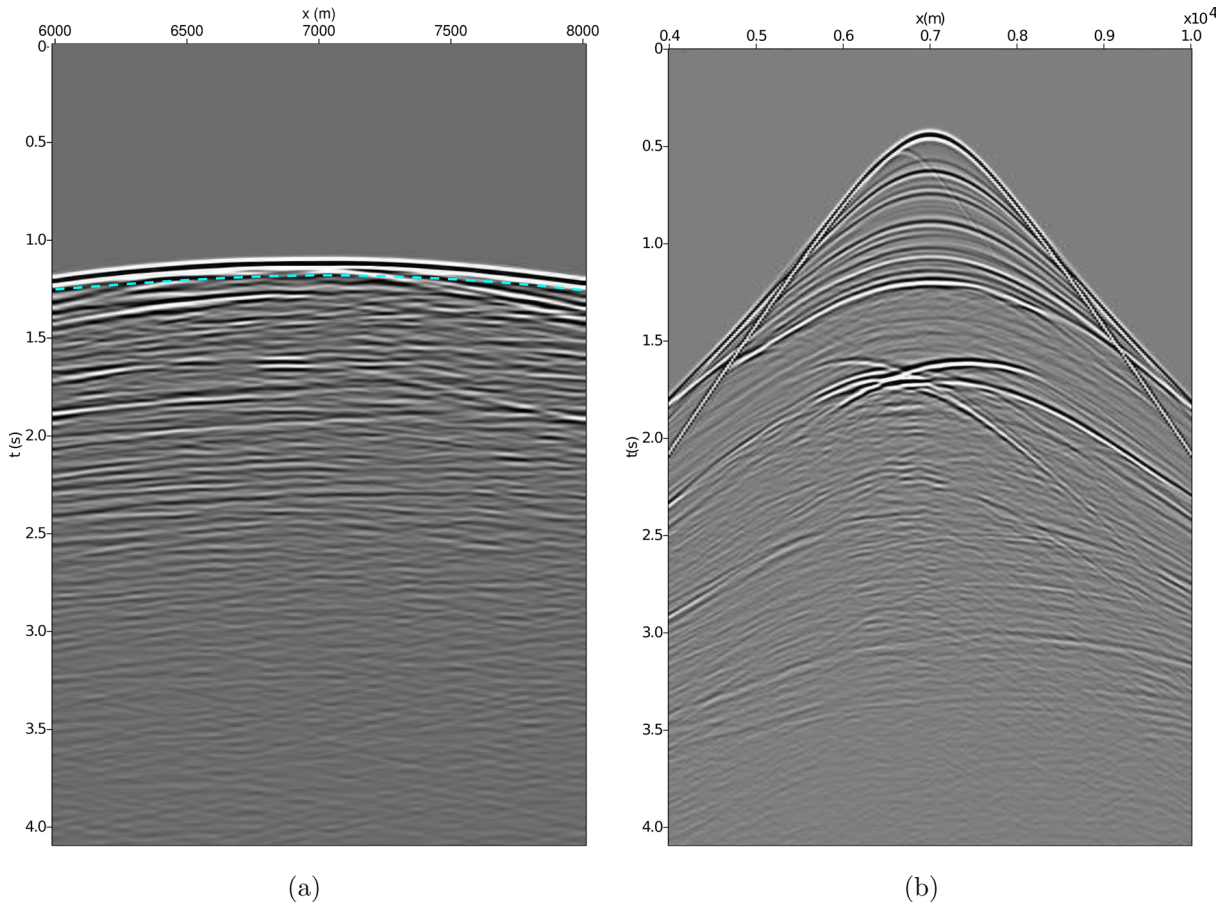

Figure 12. An example of the common-source gathers from (a) borehole data and (b) surface data (the direct arrivals are muted). The dashed line indicates the time window found by the direct arrival's traveltime.

well, but the match is already improved when the surface data are included, as seen in panel (b). This is because the left-hand side of eq. (16) contains downgoing multiples, which are not removed because the upgoing wavefield is approximated crudely by muting the direct wavefield in the total wavefield (eq. 15). With eq. (18), the upgoing wavefield is constructed by backpropagation of the surface data, so the approximation to the upgoing wavefield is improved.

Then when the focusing function is computed, most of the spurious events related to the downgoing multiples from the overburden are removed and the match is improved even more. The amplitude mismatch in the far offset traces could be because there is not a wide enough coverage of sources and receivers at the surface and in the borehole. In other words, only part of the surface integrals can be computed in practice because of the limited data acquisition apertures, but nevertheless, the kinematics of the reflections is retrieved as long as the stationary phase positions are covered in the input data (Snieder *et al.* 2006). Actually, in Fig. 14 (b), all primaries and multiples matches well in both traveltime and amplitude. These results verify the suggested redatuming schemes.

3.2.2 Target images

We first test the target images using the correct local velocities. The corresponding images from above and from below are shown in Figs 15 and 16, respectively. For the images from above in Fig. 15, all four images show the nearby reflectors. Panel (c) is the best focused and shows more details because the downgoing multiples from the overburden are removed. This is even more obvious in Fig. 16(b), the images from below, where all upgoing multiples from the underburden are removed, and the shallow structures can be seen clearly.

Next, Fig. 17(a) combines the target images in Figs 15(c) and 16(b) and plots them over the true velocity model. Panel (b) shows the conventional surface image migrated with the correct velocities. Even with the correct velocities, we can see that the surface image of the area $z > 2$ km is disturbed by the internal multiples from the 'seagull', while the target images show the structures in the same area more clearly and continuously.

Again, to test how the target images change when the wrong velocities are used, a linear 1-D velocity model is used to migrate both the redatumed responses and the original surface data set. The comparison is shown in Fig. 18, where the arrow highlights an example of the effect from internal multiples. From these two tests with different migration velocity models, we see that the target images are robust to erroneous velocities and provide clearer reflectors near the borehole than the surface image, and that the imprint of the internal multiples are less pronounced. Another point is that one actually does not need the velocity model of the overburden at all for imaging below the borehole level, as explained in the imaging from above subsection. Nevertheless, this is not to say that a good velocity model is not important. We merely suggest that one may be able to start with a more crude model and still get some focusing near the boreholes, and then later improve the velocity model with standard techniques.

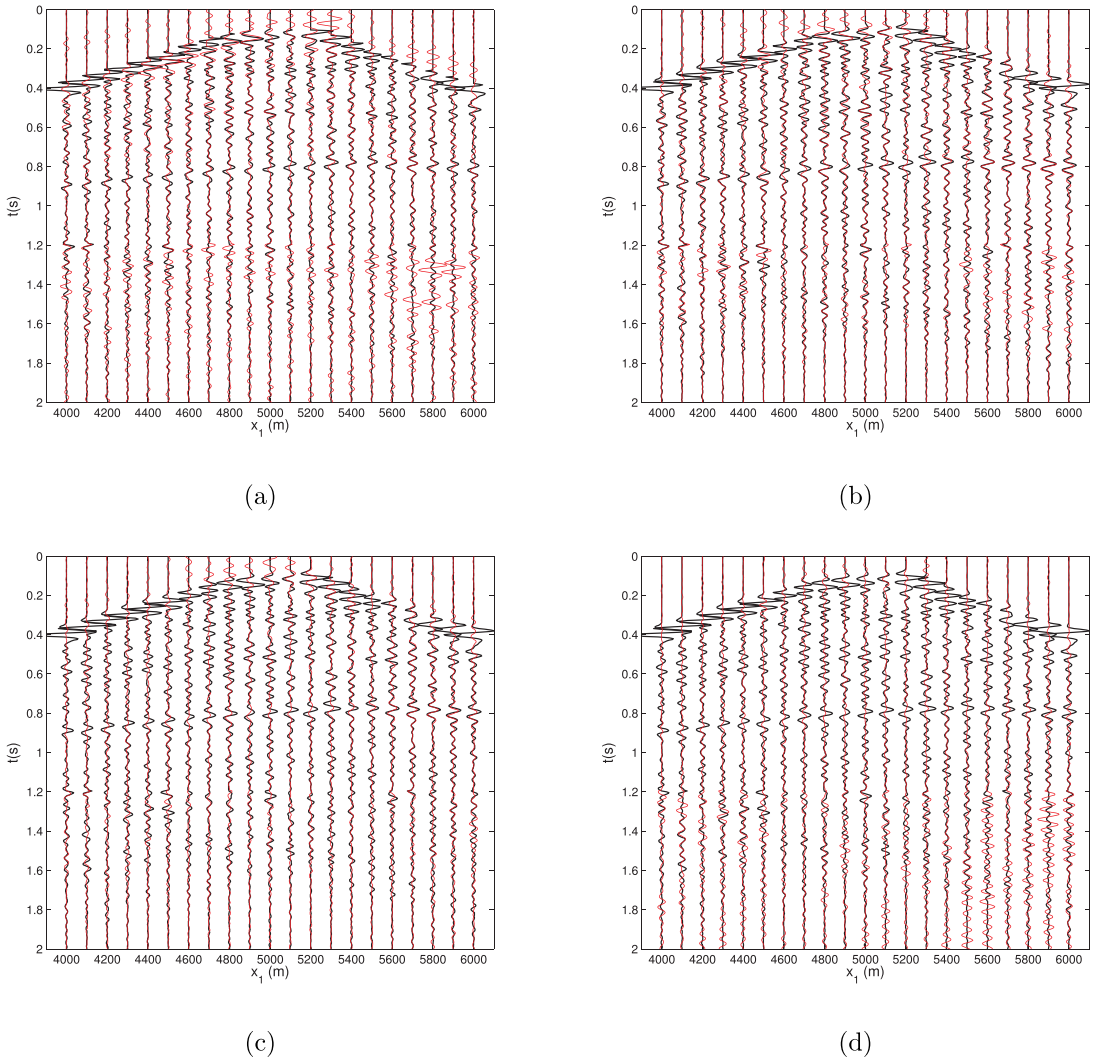

Figure 13. Redatumed reflection responses for imaging from above, using the same schemes as for Fig. 5. The reference source position is at $x = 7000$ m at 2.3 km depth and the receiver positions are from $x = 6000$ to $x = 8000$ m at the same depth as the virtual source. An overall scale is applied on the retrieved responses and a local extra scalar factor is applied for $t > 1.2$ s onward to emphasize the multiples. Every fourth trace is plotted.

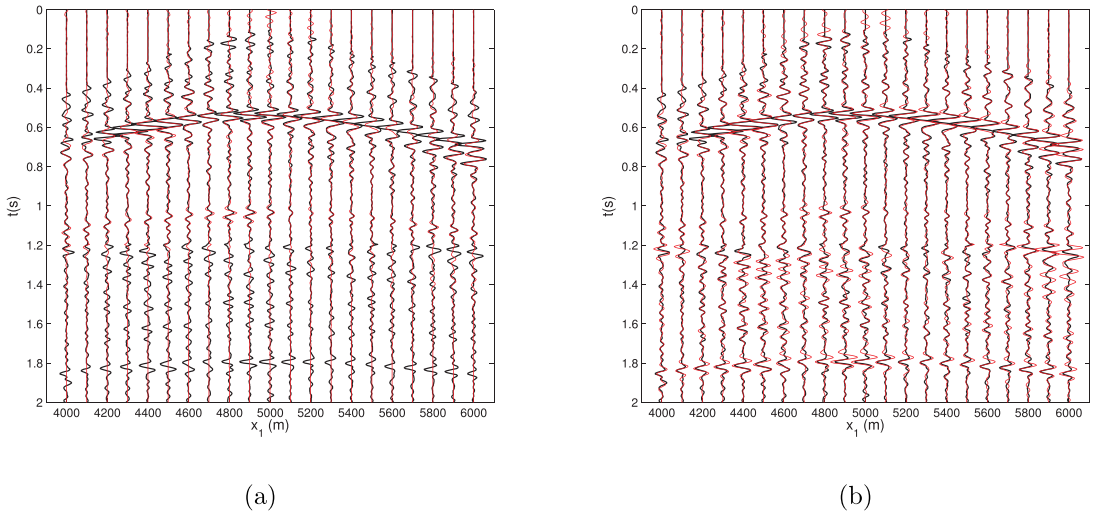

Figure 14. Redatumed reflection responses for imaging from below, using the same schemes as for Fig. 6. The reference source and receiver positions are the same as for Fig. 13. An overall scale is applied on the retrieved responses and a local gain is applied for $t > 1.2$ s to amplify the multiples. Every fourth trace is plotted.

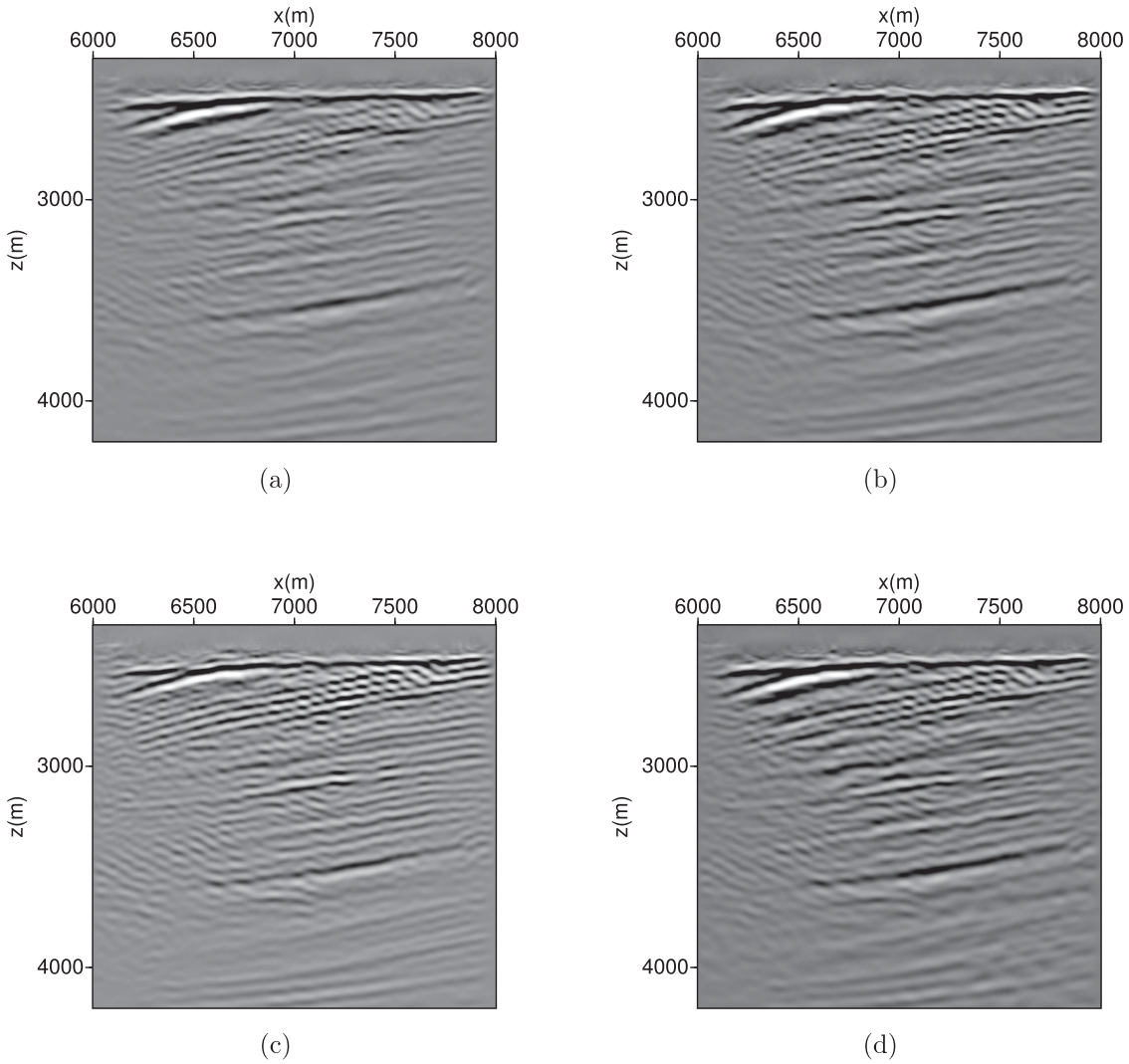

Figure 15. Migrated images from above with the correct local velocities. The data for migration are redatumed from (a) the borehole data only scheme (eq. 16), (b) the borehole and surface data scheme without the full focusing functions (18), (c) as (b) but with the correct focusing functions (eq. 17) and (d) the joint scheme of (a) and (b) (eq. 19).

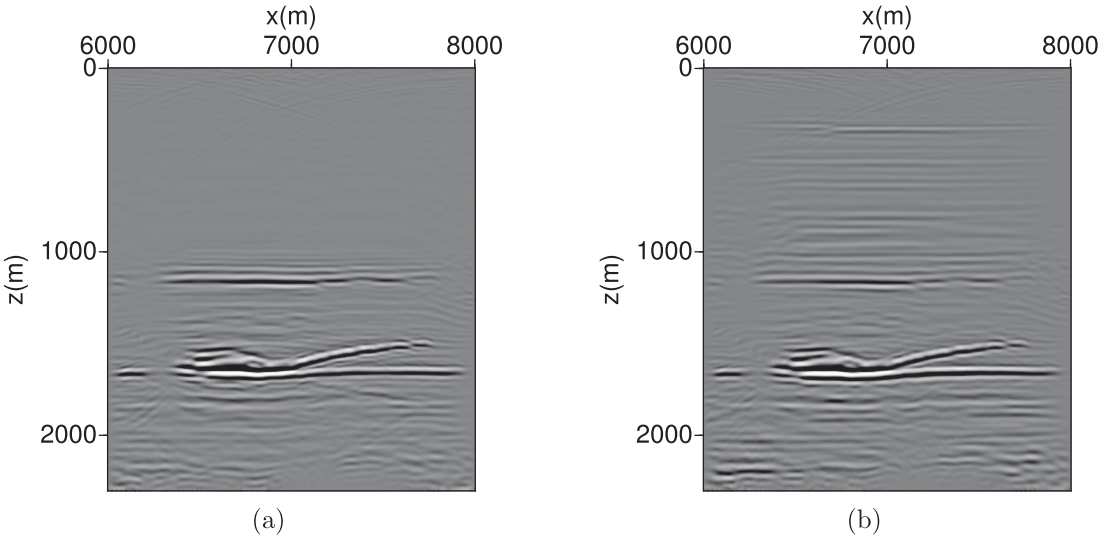

Figure 16. Migrated images from below with the correct local velocities. The data for migration are redatumed from (a) the borehole and surface data scheme without the full focusing functions (eq. 22), (b) as (a) but with the full focusing functions (eq. 21).

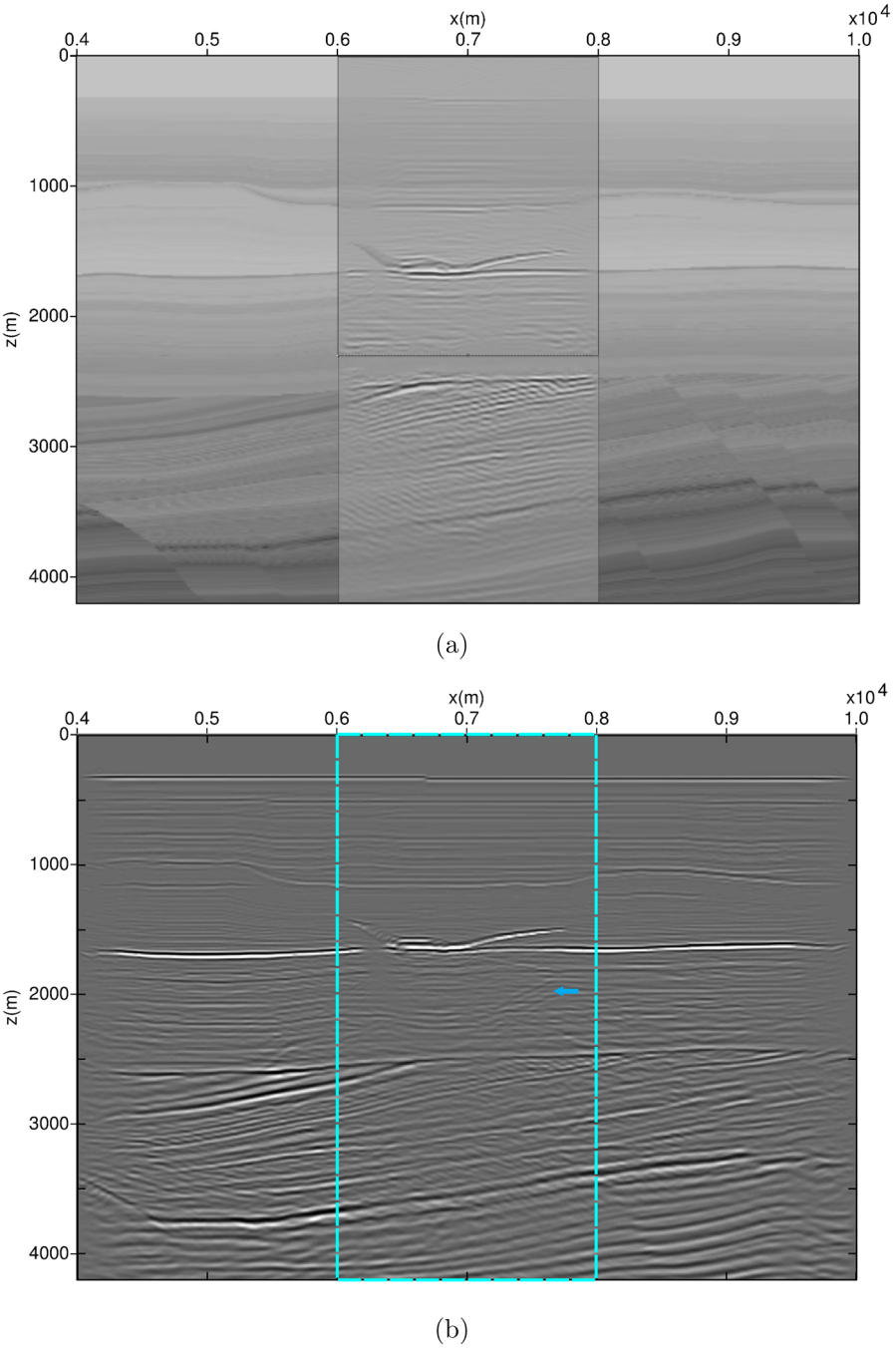

Figure 17. Image comparison of (a) target images from the redatumed data using the focusing functions (eqs 17 and 21) and (b) surface image from original surface reflection data. The dashed box highlights the target area. The arrow indicates an example of the artefacts from internal multiples. A true velocity model is used for migration.

4 DISCUSSION

As demonstrated in the numerical examples, the redatuming schemes remove part of the internal multiples. The multiples from the target zone still remain, since only the multiples from the opposite side of the target zone are removed. This results in an improvement in the images produced as seen in the numerical examples, especially when the velocity model is wrong. Because internal multiples tend to stack out destructively when a good velocity model is available, and when the velocities are wrong, the primaries interfere less constructively and the imprint from the internal multiples becomes more pronounced. For this reason, our redatuming schemes prior to the imaging step can be particularly beneficial for areas with strong multiples and velocity uncertainties.

A wide enough acquisition aperture in the input data is important, because all stationary phase positions for the target zone need to be covered. In our test, since only a 20 Hz Ricker wavelet is used for modelling the borehole data, the resolution of the images is limited and could be improved if higher frequencies are used. For the surface data, in order to find the correct focusing function, we model the

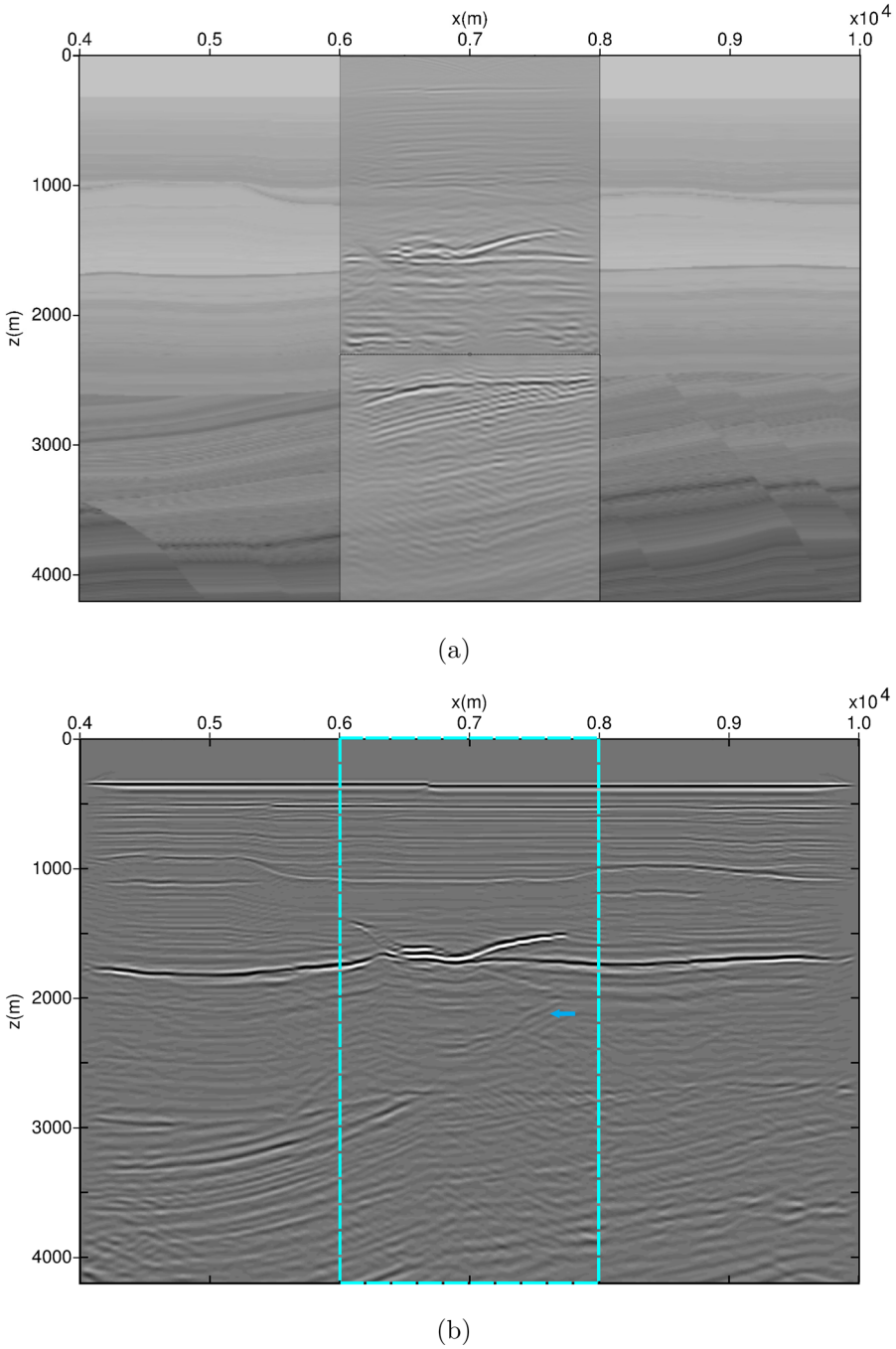

Figure 18. Image comparison of (a) target images from the redatumed results and (b) surface image from original surface reflection data. The dashed box highlights the target area. The arrow indicates an example of the artefacts from internal multiples, which become more pronounced given the wrong velocity model. These artefacts are absent in the target image in panel (a). A simple 1-D linear velocity model is used for migration.

reflection response to an input spike, but for data acquired in the field, they correspond to the Green's function convolved with the source signature. Therefore, a good source signal estimation is required in practice in order to take full advantage of the schemes presented. The proposed alternative schemes do not have this requirement and are often still sufficient solutions for imaging local geological structures in the presence of velocity errors in the model, as shown in the experiments.

The schemes as presented assume that the borehole is at a constant depth, but the method can be immediately adapted to include non-horizontal boreholes by extrapolating the direct arrivals in the borehole data to a constant depth using the forward Kirchhoff–Helmholtz integral (Wapenaar 1993). The extension to retrieve the reflection response defined locally according to the borehole orientation, however, still needs to be investigated. The surface related multiples are not considered in the schemes, but Singh *et al.* (2015) show how to take them in account in the Marchenko method, so this can also be done here. Another suggestion for future study is the possibility of using more than the direct arrivals in the borehole data for finding the focusing functions, and this is currently

being investigated. It is also observed that images from the surface and from the borehole (when imaging from below) inherit a different sensitivity to errors in the velocity model. Similar observations have also been made by Ravasi *et al.* (2015a) and might be used for updating the velocity model.

5 CONCLUSIONS

We present a novel application of SI and Marchenko imaging, using both surface and borehole seismic data. A series of redatuming schemes that require only single-component data are presented to create virtual data sets with both sources and receivers in the borehole. These virtual data sets are ideal for deep target imaging near the borehole, because the medium properties in the shallower part become irrelevant when imaging using these data sets and the virtual sources and receivers are close to the target area. Furthermore, cleaner and more accurate images are obtained because the interfering internal multiples from the overburden and underburden are removed in the redatuming schemes. Finally, the numerical experiments also show that these images are more robust to velocity errors in the model than conventional surface images. Good deep target images are obtained with simple velocity input after applying these redatuming schemes.

ACKNOWLEDGEMENTS

The authors acknowledge the Research Council of Norway, ConocoPhillips, Det norske oljeselskap, Statoil, Talisman, TOTAL and Wintershall for financing the work through the research centre DrillWell – Drilling and Well Centre for Improved Recovery. The contribution of Joost van der Neut is financially supported by the Dutch Technology Foundation (grant VENI.13078). We also like to acknowledge the ROSE consortium at NTNU, Jan Thorbecke at TU Delft and Alexander Kritski at Statoil for the field velocity model. We appreciate the review and comments of Rene-Edouard Plessix, the Editor, and Filippo Broggini, which helped improve this paper.

REFERENCES

Amundsen, L., 1993. Wavenumber-based filtering of marine point-source data, *Geophysics,* **58**(9), 1335–1348.

Amundsen, L., 2001. Elimination of free-surface related multiples without need of the source wavelet, *Geophysics,* **66**(1), 327–341.

Amundsen, L. & Reitan, A., 1995. Decomposition of multicomponent seafloor data into upgoing and downgoing p- and s-waves, *Geophysics,* **60**(2), 563–572.

Bakulin, A. & Calvert, R., 2006. The virtual source method: theory and case study, *Geophysics,* **71**(4), SI139–SI150.

Behura, J., Wapenaar, K. & Snieder, R., 2014. Autofocus imaging: image reconstruction based on inverse scattering theory, *Geophysics,* **79**(3), A19–A26.

Broggini, F., Snieder, R. & Wapenaar, K., 2012. Focusing the wavefield inside an unknown 1d medium: beyond seismic interferometry, *Geophysics,* **77**(5), A25–A28.

Claerbout, J., 1968. Syntnoise of a layered medium from its acoustic transmission response, *Geophysics,* **33,** 264–269.

Curtis, A. & Halliday, D., 2010. Source-receiver wave field interferometry, *Phys. Rev. E,* **81**(4), 046601, doi:10.1103/PhysRevE.81.046601.

Curtis, A., Gerstoft, P., Sato, H., Snieder, R. & Wapenaar, K., 2006. Seismic interferometry—turning noise into signal, *Leading Edge,* **25**(9), 1082–1092.

Curtis, A., Nicolson, H., Halliday, D., Trampert, J. & Baptie, B., 2009. Virtual seismometers in the subsurface of the Earth from seismic interferometry, *Nature Geosci.,* **2**(10), 700–704.

Duvall, T.L., Jefferies, S.M., Harvey, J.W. & Pomerantz, M.A., 1993. Time-distance helioseismology, *Nature,* **362**(6419), 430–432.

Galetti, E. & Curtis, A., 2012. Generalised receiver functions and seismic interferometry, *Tectonophysics,* **532–535**(0), 1–26.

Liu, Y., Draganov, D., Wapenaar, K. & Arntsen, B., 2016. Retrieving virtual reflection responses at drill-bit positions using seismic interferometry with drill-bit noise, *Geophys. Prospect.,* **64**(2), 348–360.

Meles, G.A., Löer, K., Ravasi, M., Curtis, A. & da Costa Filho, C.A., 2015. Internal multiple prediction and removal using marchenko autofocusing and seismic interferometry, *Geophysics,* **80**(1), A7–A11.

Menke, W., 1989. *Geophysical Data Analysis: Discrete Inverse Theory,* Academic Press.

Minato, S., Matsuoka, T., Tsuji, T., Draganov, D., Hunziker, J. & Wapenaar, K., 2011. Seismic interferometry using multidimensional deconvolution and crosscorrelation for crosswell seismic reflection data without borehole sources, *Geophysics,* **76**(1), SA19–SA34.

Poliannikov, O., 2011. Retrieving reflections by source–receiver wavefield interferometry, *Geophysics,* **76**(1), SA1–SA8.

Ravasi, M., Vasconcelos, I., Curtis, A. & Meles, G., 2015a. Elastic extended images and velocity-sensitive objective functions using ultiple reflections and transmissions, *Geophys. J. Int.,* **202,** 943–960.

Ravasi, M., Vasconcelos, I., Kritski, A., Curtis, A., da Costa Filho, C.A. & Meles, G.A., 2015b. Marchenko imaging of volve field, north sea, in *77th EAGE Conference and Exhibition, Extended Abstracts,* doi:10.3997/2214-4609.201412938.

Ravasi, M., Vasconcelos, I., Kritski, A., Curtis, A., da Costa Filho, C.A. & Meles, G.A., 2016. Target-oriented Marchenko imaging of a North Sea field, *Geophys. J. Int.,* **205**(1), 99–104.

Schuster, G.T., 2009. *Seismic Interferometry,* Cambridge University Press.

Schuster, G.T., Yu, J., Sheng, J. & Rickett, J., 2004. Interferometric/daylight seismic imaging, *Geophys. J. Int.,* **157**(2), 838–852.

Singh, S., Snieder, R., Behura, J., van Der Neut, J., Wapenaar, K. & Slob, E., 2015. Autofocusing imaging: imaging with primaries, internal multiples and free-surface multiples, *Geophysics,* **80**(5), S165–S174.

Snieder, R., Wapenaar, K. & Larner, K., 2006. Spurious multiples in seismic interferometry of primaries, *Geophysics,* **71**(4), SI111–SI124.

Snieder, R., Miyazawa, M., Slob, E., Vasconcelos, I. & Wapenaar, K., 2009. A comparison of strategies for seismic interferometry, *Surv. Geophys.,* **30**(4–5), 503–523.

Thorbecke, J. & Draganov, D., 2011. Finite-difference modeling experiments for seismic interferometry, *Geophysics,* **76**(6), H1–H18.

Thorbecke, J., Wapenaar, K. & Swinnen, G., 2004. Design of one-way wavefield extrapolation operators, using smooth functions in WLSQ optimization, *Geophysics,* **69**(4), 1037–1045.

van der Neut, J. & Wapenaar, K., 2015. Point-spread functions for interferometric imaging, *Geophys. Prospect.,* **63**(5), 1033–1049.

van der Neut, J., Alexandrov, D. & Bakulin, A., 2016. Shallow virtual source redatuming by multi-dimensional deconvolution, *Geophys. Prospect.,* **64**(1), 4–18.

van der Neut, J., Wapenaar, K., Thorbecke, J. & Slob, E., 2015. Practical challenges in adaptive Marchenko imaging, in *SEG Technical Program Expanded Abstracts 2015,* pp. 4505–4509.

Vasconcelos, I. & Snieder, R., 2008a. Interferometry by deconvolution: Part 1—Theory for acoustic waves and numerical examples, *Geophysics,* **73**(3), S115–S128.

Vasconcelos, I. & Snieder, R., 2008b. Interferometry by deconvolution: Part 2—Theory for elastic waves and application to drill-bit seismic imaging, *Geophysics,* **73**(3), S129–S141.

Wapenaar, C.P.A., 1993. Kirchhoff–Helmholtz downward extrapolation in a layered medium with curved interfaces, *Geophys. J. Int.,* **115**(2), 445–455.

Wapenaar, K., 2004. Retrieving the elastodynamic Green's function of an arbitrary inhomogeneous medium by cross correlation, *Phys. Rev. Lett.,* **93**(25), 254301, doi:10.1103/PhysRevLett.93.254301.

Wapenaar, K. & van der Neut, J., 2010. A representation for Green's function retrieval by multidimensional deconvolution, *J. acoust. Soc. Am.,* **128**(6), EL366–EL371.

Wapenaar, K., van der Neut, J., Ruigrok, E., Draganov, D., Hunziker, J., Slob, E., Thorbecke, J. & Snieder, R., 2011. Seismic interferometry by

crosscorrelation and by multidimensional deconvolution: a systematic comparison, *Geophys. J. Int.,* **185**(3), 1335–1364.

Wapenaar, K., Broggini, F., Slob, E. & Snieder, R., 2013. Three-dimensional single-sided Marchenko inverse scattering, data-driven focusing, Green's function retrieval, and their mutual relations, *Phys. Rev. Lett.,* **110**(8), 084301, doi:10.1103/PhysRevLett.110.084301.

Wapenaar, K., Thorbecke, J., van der Neut, J., Broggini, F., Slob, E. & Snieder, R., 2014. Marchenko imaging, *Geophysics,* **79**(3), WA39–WA57.

Willis, M., Lu, R., Campman, X., Nafi Toksz, M., Zhang, Y. & Hoop, M., 2006. A novel application of time-reversed acoustics: salt-dome flank imaging using walkaway VSP surveys, *Geophysics,* **71**(2), A7–A11.